LOW TEMPERATURE MANUFACTURING OF FERRITE-EPOXY INDUCTOR CORES BY MICRO-ROBOTIC DEPOSITION

BY

SPENCER SCOTT IGRAM

THESIS

Submitted in partial fulfillment of the requirements
for the degree of Master of Science in Mechanical Engineering
in the Graduate College of the
University of Illinois at Urbana-Champaign, 2018

Urbana, Illinois

Adviser:

Professor Andrew Alleyne

Abstract

Inductors and transformers are an important class of passive components in high and pulsed power electronics. Inductive type elements such as these are useful in energy storage, pulse shaping or filtering, and power conversion. These devices are made up of two major components; the conductive windings that provide the inductive properties, and the magnetic cores used to enhance those properties. Power losses associated with these devices can also be categorized by these two components called copper and iron losses, respectively. Iron losses, or core losses, are highly dependent on the materials used and the manufacturing method for the core. Losses come in the form of thermal energy accumulated in the core itself. These devices, which can represent a plurality or even majority composition of power electronics circuitry, pose a significant challenge and opportunity to improve power density capabilities in high and pulsed power electronics.

This thesis discusses manufacturing magnetic cores at low temperature (<100 °C) and a control method for the manufacturing system. The manufacturing system of interest is micro-Robotic Deposition (μRD), a three-axis material extrusion type additive manufacturing system. The choice of this manufacturing method greatly influences the rheological properties required of the composite inks used for target components. A ferrite-epoxy composite ink consisting of micron-sized carbonyl iron powder and a common industrial epoxy matrix, Bisphenol-A diglycidyl ether (DGEBA)/ Diethylene Triamine (DETA), is used with a rheology modifier to achieve the proper rheology profile of the magnetic ink.

A velocity centric PID control strategy is implemented on each axis of the μRD system to achieve proper motion and position control of the manufacturing process. Results show good

control performance across printing speeds of 1-25 mm/s, as determined by biaxial contour mappings. Components manufactured from the composite provided hold the desired topology, indicating proper rheological tuning of the ink material, and were fully cured in under 8 hours at ambient room conditions (~23 ℃).

To my family

Acknowledgements

First and foremost, I must thank Professor Andrew Alleyne for the support and guidance he has given me from day one. The opportunity to work so closely with a researcher and thinker of his caliber has been nothing less than a privilege. Professor Alleyne puts the future and wellbeing of his students above all else and has taught me more about being a good role model and person than I could have ever expected or asked for.

I would like to thank Dr. Dale Huber and Dr. John Watt from Sandia National Laboratories for their help with the materials systems developed in this thesis. Dale was nothing less than supportive of my desire to try new methods or materials along the way. John likewise is always willing to talk with me about the finer details of the chemistries involved and help in fine tuning much of the stoichiometry used in this work. I must also thank them both for the immense hospitality they showed when I came to visit the Center for Integrated Nano-Technologies facility my first year.

To all the members of the Alleyne Research Group (ARG), I cannot thank you enough for the sense of community you impart into the graduate experience here at Illinois. To the more senior members of the lab, Justin, Matt, Herschel and now Donald, I will continue to value the advice and wisdom you gave me throughout the years and on our coffee walks. Malia, Oyuna, Ashley, Pamela, Nate, and Spencer K. (AKA – O.G. Spencer), thank you all for being such a fun-loving cohort just a year ahead of me. Sarah and Sunny, two of my closest friends those first few years as the S-cubed cohort, I will never forget all the fun we had in and out of lab – especially at C Street. Thanks to Chris and Cary, the newest ARG recruits, for continuing the traditions of community and support for one another that ARG is so well known for.

Table of Contents

List of Figures

List of Tables

Chapter 1
Introduction

The process by which a three-dimensional part or object is manufactured can be categorized into one of the three methodologies: 1) Subtractive Manufacturing (SM), 2) Forming Manufacturing (FM), or 3) Additive Manufacturing (AM) [1]. A brief description and sample process within SM and FM are given in the next two subsections, while a deeper discussion on AM follows in the sections thereafter.

1.1 Subtractive Manufacturing

Subtractive manufacturing is the modern naming convention applied to the traditional manufacturing processes, such as machining and milling, due to the recent decade's upswing in commercialized additive manufacturing technologies. The overarching theme connecting all SM processes is the controlled removal of material from a bulk source to create a final product. The single most commonly used form of SM is Computer Numerical Control (CNC) machining [2].

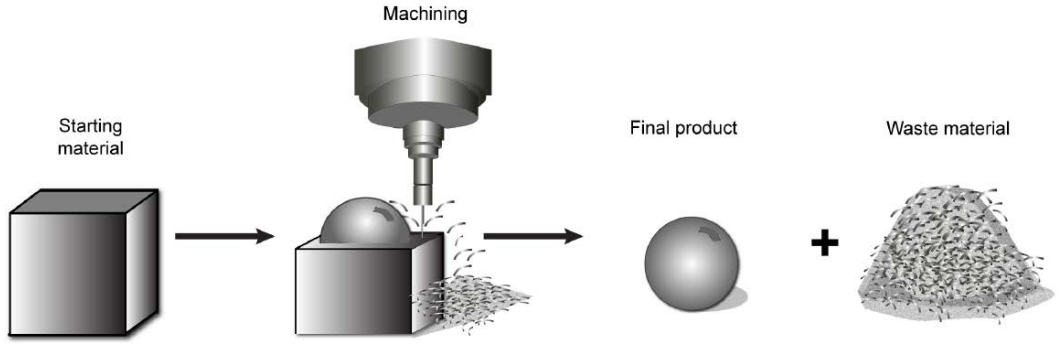

Figure 1.1 A conceptual outline of the subtractive manufacturing process [3]

1.2 Forming Manufacturing

Forming manufacturing encompasses any process by which the target material(s) are placed into a predesigned mold or cavity with the desired shape of the final product. A specific method of FM commonly used in the manufacturing of soft-ferrites, powder injection molding (PIM), leverages the workability of plastics while incorporating metals and/or ceramics for their superior mechanical properties to form components [4]–[6]. Metal and/or ceramic powder(s) are combined with an organic binder – often some form of thermoplastic/ polymeric-solvent blend – to create what is known as the feedstock. The homogenized feedstock is then injected into the desired mold through an auger/screw conveyer system [4] as diagramed in Figure 1.2. After the mold has been filled and cooled, the organic binder is removed in a two-step sub-process called debinding.

The specific chemistry of the binding material greatly influences the type of debinding process that occurs. Typically, part of the binding material is dissolved away through either a solvent bath, or volatilization methods and the residual organic component is thermally decomposed, leaving a powdery metal/ceramic composition in the form of the mold. Once debinding has occurred, the remaining part is sintered – heating at extreme temperatures, often several hundreds of degrees Celsius – in order to fuse the particulate constituents together, forming the final part.

Careful attention must be paid to the sintering environment because of the extreme temperatures to prevent adverse oxidization or reduction of the part. For example, metallic powders such as Iron and Stainless Steel typically require inert or reducing atmospheres (i.e. hydrogen gas) or high vacuum; on the other hand, ceramic oxides are sintered in air [4], [5]. Nearly all parts that go through a sintering process to be manufactured result in a considerable amount of shrinkage in the final production – usually 10-20% [4], [5] compared to the pre-sintered dimensions. In general, manufacturers must compensate for these discrepancies in advance by directionally over/under sizing their molds according to the specific thermal expansion/shrinkage of the material.

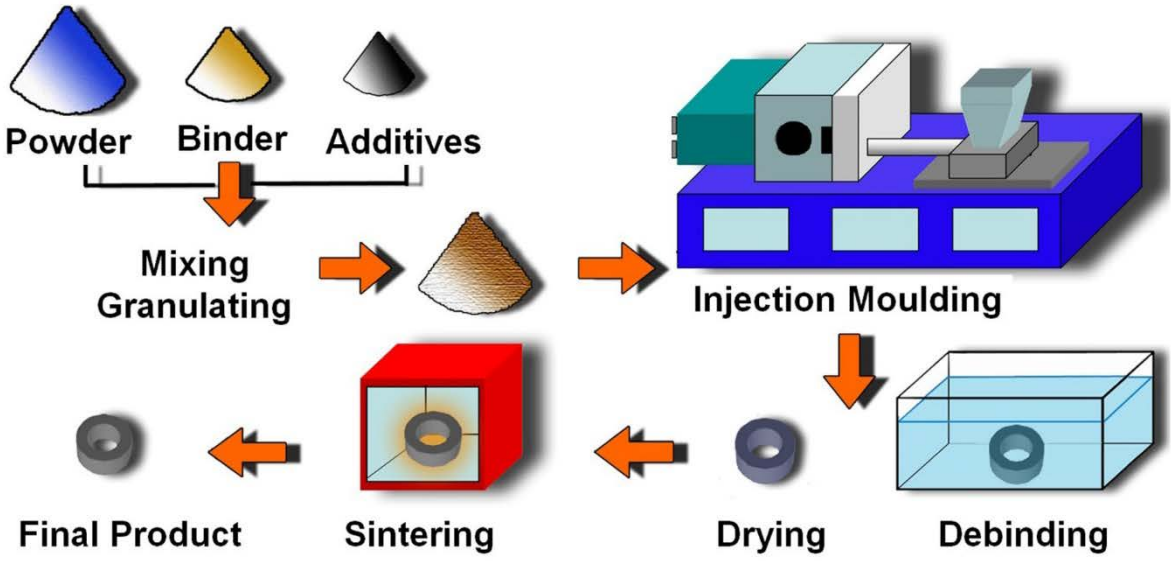

Figure 1.2 Powder Injection Molding process [7]

1.3 Additive Manufacturing

Additive Manufacturing (AM) is defined as any process involving the translation of 3D model data into physical parts by the joining together of materials [8]. With more than 10% growth as an industry for 18 of the past 27 years and over 300 companies/start-ups/etc. now offering an affordable introductory or desktop sized model (units costing less than $5K) [9], AM has gone from "a promising set of uncommercialized technologies in the early 1980s to a market that was worth over $4 billion in 2014" [10]. Commonly referred to as 3D printing, rapid prototyping, or solid freeform [11]; the potential for reducing material costs, increasing production speeds, and creation of on-demand, customizable, functional parts are all contributing factors to the accelerating rise in popularity for AM technologies among DIY enthusiasts, industrial behemoths such as Boeing, and academic institutions. By 2020, 3D printing is expected to have a market place value of more than $21 billion [10].

Biomedical applications – specifically dental implants, crowns and bridges – are currently the fastest growing sectors of an already impressively spreading technology, even creating 3D printed ceramic and/or metallic constructs [1]. In aerospace component manufacturing, the increased ability to realize optimal component designs, provided by AM, can create substantial savings by reducing material waste (by as much as 90% in some cases)

and overall mass per part [12]. Further improvements to available methods, the technologies they rely upon, and increasingly advanced materials for AM will be needed as companies and consumers continue to demand shorter product development cycles and lead times, increasing customization of products, reduced manufacturing costs and sustainability considerations [10], [13], [14].

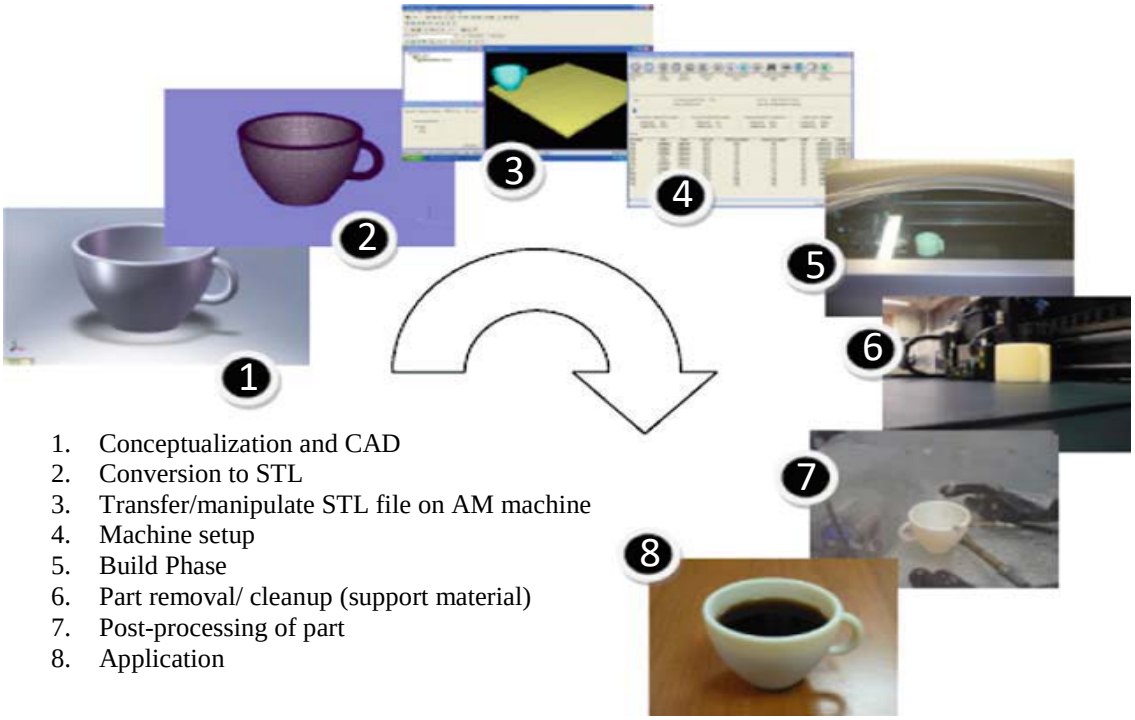

Figure 1.3 Eight step process to go from concept to reality for additive manufacturing technologies [15]

1.3.1 Various AM Techniques

The earliest forms of AM developed as techniques to allow fabrication of moderately-complex conceptual designs. Today, several different methods of 3D printing are implemented by engineers to produce low cost, high resolution prototypes from computer-aided design (CAD) models – commonly referred to as Rapid Prototyping (RP) [1], [11], [12], [16]. Gibson et al. [15] describe a general eight part process to go from concept to part for all AM methods which is depicted in Figure 1.3.

AM methods create objects by adding materials to reduce waste while reaching satisfactory geometric accuracy [12]. These technologies are traditionally separated into seven categories: (1) sheet lamination; (2) vat photopolymerization; (3) powder bed fusion; (4) binder jetting; (5) material jetting; (6) directed energy deposition (7) material extrusion. Any AM process shares the common principle of adding material(s) for the purpose of building components; whether that comes by depositing binding agents, initiating chemical reactions, sintering of metal/ceramic powders, or extruding filaments of polymer [17].

1.3.1.1 Sheet Lamination

The most similar additive method to Subtractive Manufacturing, sheet lamination – often called Laminated Object Manufacturing (LOM) – is typically operated in what is called a Roll-to-Roll process. The LOM feedstock is formed into thin continuous sheets that are rolled into a spindle of the material. During operation, this type of feedstock is unrolled from one end of the operation, fed to the processing/cutting stage and excess material is fed to another roll at the opposite end of the process, Figure 1.4. LOM employs a high-powered laser to cut out entire layers in specific shapes from the feedstock. Layers are then treated or "laminated" with a binding agent to adhere it to the bottom of the next layer in the build process. The build stage is then lowered, making room for the next layer and the process is repeated.

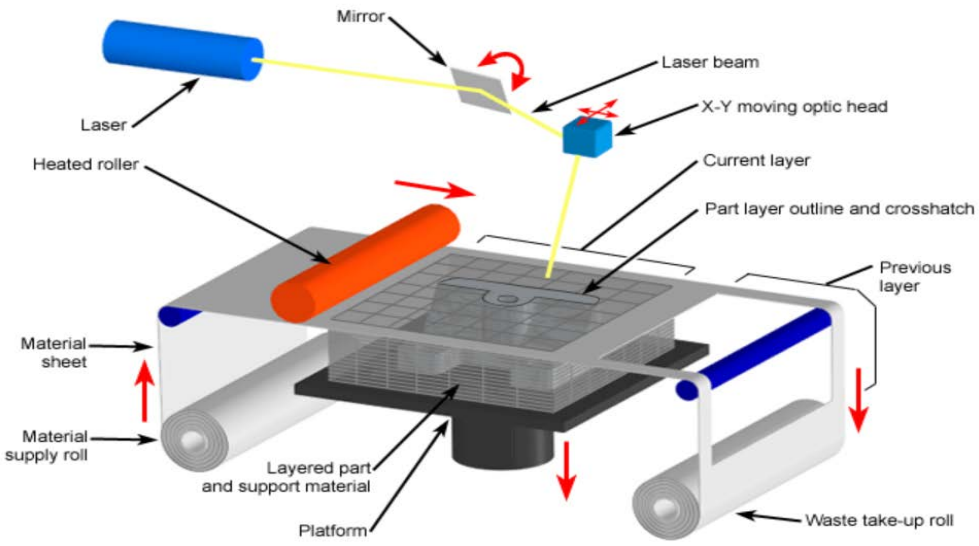

Figure 1.4 Laminated Object Manufacturing (LOM) process [18]

1.3.1.2 Vat Photopolymerization

Vat Photopolymerization is a form of AM that operates under the basic mechanism of curing or solidifying a light-reactive resin called liquid photopolymers by projecting a two-dimensional image using a specific spectrum of light onto a stage within a pool of the resin. Only the desired area of resin which comes into contact with the UV light solidifies due to a chemical reaction called Photopolymerization. Once the specified area has had time to fully react and solidify, the stage is lowered to repeat the process where the next layer's image is shown. This is repeated layer-by-layer until the part is completed. The stage is then lifted out of the pool and any remaining uncured resin is solidified by putting the part into a post-processing light chamber or removed simply by washing the part with an appropriate solvent. Stereolithography was the industry's initial consumer-level available method of RP; a type of Vat Photopolymerization "whereby a concentrated beam of ultraviolet lamp is used to solidify a liquid photopolymer by tracing a two-dimensional (2D) layer in the form of a contour and then an infill [17].

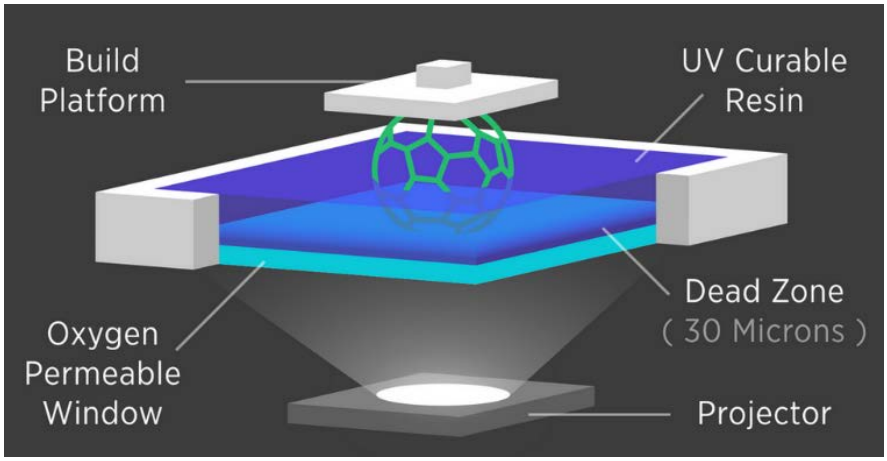

Figure 1.5 Conceptual diagram of Vat Photopolymerization process [19]

1.3.1.3 Powder Bed Fusion (SLS)

Powder Bed Fusion (PBF) methods, specifically Selective Laser Sintering (SLS), involve using a focused laser to fuse particles together from a bed of metallic powder. Once a layer has been fused together the powder bed is lowered, and new layer of powder is added

from a reservoir of material which is leveled out by a roll pin. These layers are thin enough for the laser to fuse not only the powder of the current layer but the previous layer to it as well.

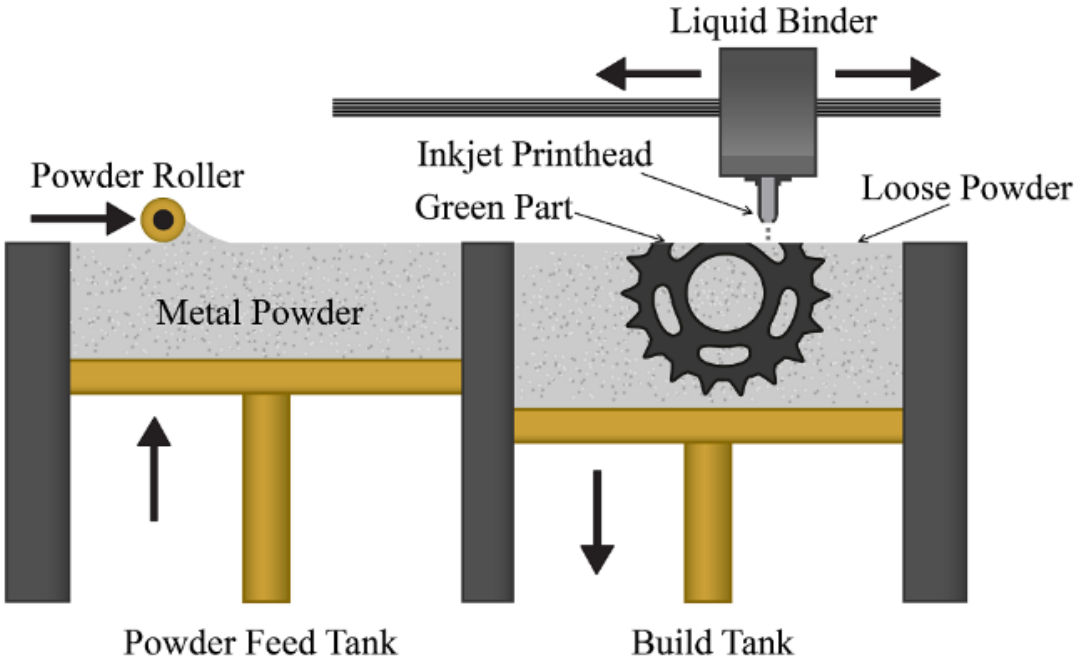

Figure 1.6 Concept design for Powder Bed Fusion and Binder Jetting methods of AM. By installing an inkjet print head depositing binder material as above is classified as Binder Jetting. Opting for a scanning laser rather than the inkjet print head is classifies the process as Powder Bed Fusion. [20]

1.3.1.4 Binder Jetting

The basic principle of Binder Jetting is nearly identical to that of PBF, the main difference being the physics of how particles are joined together from the bulk powder. This method often deposits an organic binder material (similar to PIM) at specific coordinates as opposed to the high heats generated using high-powered lasers. Depending on the binder, a UV lamp may be employed to assist in solidifying the layer.

1.3.1.5 Material Jetting

Material Jetting is a transitional technology between the aforementioned AM methods and freeform methods of AM. Similar in its deposition strategy to Binder Jetting, Material

Jetting utilizes a multi nozzle deposition head where one delivers the build material and the other selectively deposits binder material to join specific sections of the material as it follows. Once again, this method can employ UV curing lamps to help solidify parts/sections. The most significant difference in this method is the loss of a required step to add and level out an entire layer of build material. Rather, this method can operate continuously while only depositing unbound material where necessary to support the build process.

1.3.1.6 Directed Energy Deposition (DED)

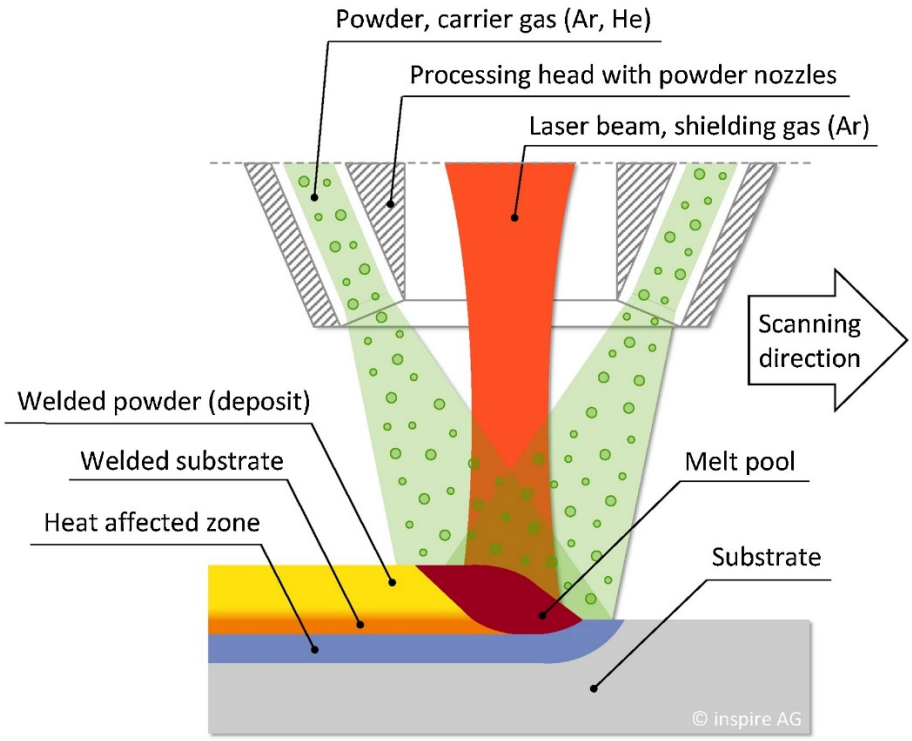

Figure 1.7 In directed energy deposition (DED), a high-power laser melts metal powder as it reaches the surface of the part, while a shield gas prevents oxidation until the metal cools and solidifies. The specialized laser head moves along the surface to build the part [21].

One of the newest forms of AM, the build process for DED differs from other beam excitation AM methods in that the material can be deposited more freely in space rather than treating or operating on a bed or sheet of preexisting bulk material. Depending on the material of choice, the feedstock can either be wire filament or fine powders which are directed from

multiple offset feed nozzles. Each feed nozzle directs the material towards the center of the deposition where a high-powered laser or concentrated electron beam melts and/or fuses the material in place. Under this method, a multi-axis robot is used to control the three-dimensional position of the deposition head to manage the continuous freeform building or repair of parts.

1.3.1.7 Material Extrusion

According to Kim et al. [22], material extrusion is the class of continuous freeform AM "in which material is pushed out through a nozzle when a constant pressure is applied. The extruded material will deposit at a constant speed and fully solidify on the substrate after it comes out of the nozzle. In addition, the material must bind with previous material so that a solid part can form and [retain its] structure throughout the process."

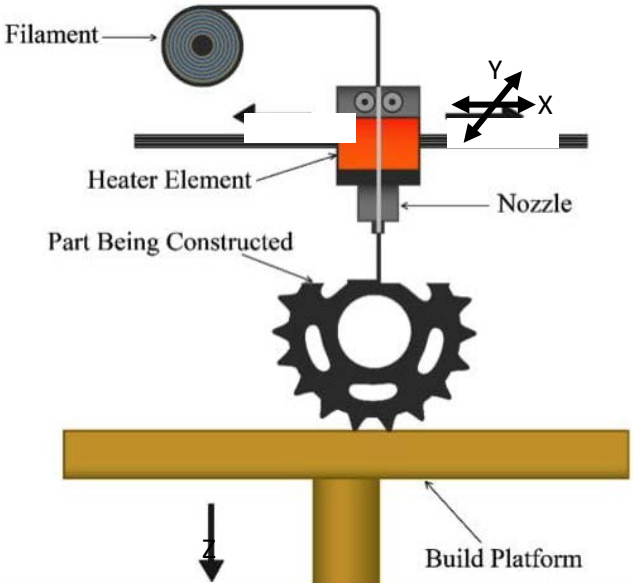

Figure 1.8 Depiction of a typical FDM process (derived from [23])

Fused Deposition Modeling (FDM) is currently the most widely recognized and commercially used form of material extrusion and 3D printing in general. FDM takes in solid filaments of thermoplastic polymers such as polylactic acid (PLA) and Acrylonitrile butadiene styrene (ABS). Gears feed it through a heated chamber/nozzle where the polymer is heated to just above its melting point so it can be extruded through the nozzle in a fluid state. These plastics can rapidly solidify within a fraction of a second after being extruded allowing it to

form continuous layers and solid parts quite effectively and fairly quickly. Due to the relatively low cost of raw materials and consumer level set-ups, vast open source availability of user interfaces, and the relatively straightforward 'melt-apply-solidify' approach, FDM has become the most widely adopted RP method, especially among hobbyists and startups [12]. FDM is somewhat limited in its breadth of available materials, only being applicable to thermoplastic matrices. A more traditional and diverse form of material extrusion is 3D Plotting.

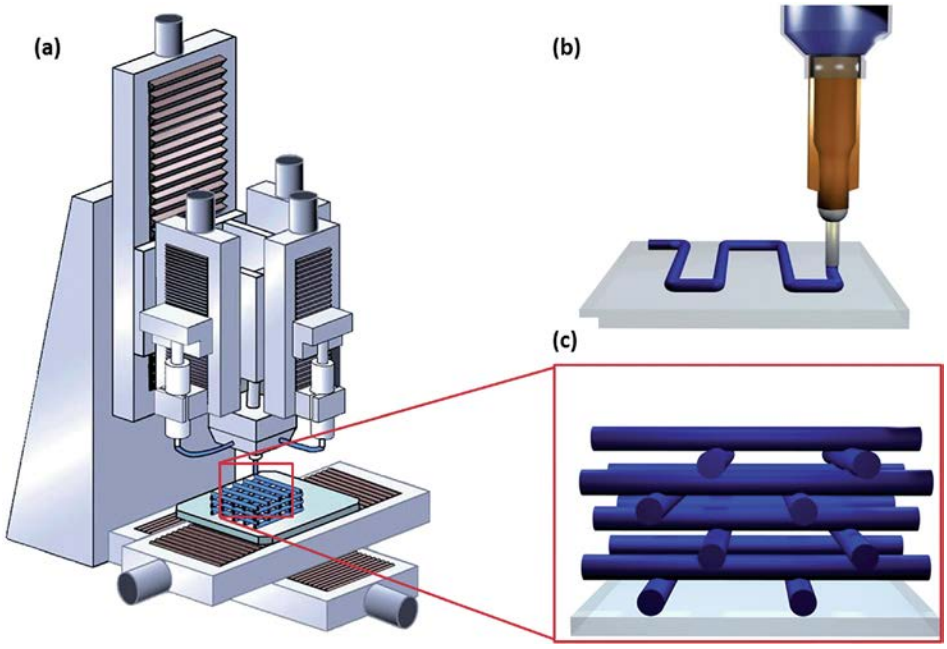

Figure 1.9 General Material Extrusion (i.e. Material Plotting/Robocasting) system; a) the computer controlled XYZ positioning robot, b) controlled extrusion of ink to substrate, c) cross-sectional view of a multi-layered periodic structure [24]. Material plotting differs from FDM in that there is no heating element needed for the extrusion nozzle.

In 3D plotting, a viscous material is pneumatically or mechanically extruded from a syringe through a sub-millimeter gauge nozzle creating a multitude of products. The syringe is typically attached to the z-axis of a 3-4 axis stage moving freely in all three dimensions while material is deposited to a stationary substrate [25]. If the necessary viscosity is not achieved by the nature of the material itself, thixotropic fillers are used to yield a desired pseudoplastic flow behavior, which in turn creates "a filament that can be rapidly solidified in place based

on gelation reaction, drying or photopolymerization" [26]. The quality and resolution of parts can be related to the final material viscosity and speed at which it is deposited [27]. A major advantage to 3D plotting is the inherent material flexibility, albeit at the cost of very specialized material design by application.

1.4. Materials used in AM

Materials are historically grouped into 4 major classes: Metals, Ceramics, Polymers, and Composites. This work collects these first three material categories into the group of "pure" materials as to focus on the differences between these pure materials vs. composites with respect to the AM space.

1.4.1 Pure Materials in AM

Both metals and ceramics have highly desirable mechanical and thermal properties along with long vetted end-use functionality across a multitude of application domains within manufacturing. However, 3D printed components from purely metallic or ceramic build materials remain extremely rare. The main method utilized for this is PBF. While the selective sintering of powders from the bed of material allows for the layer-by-layer construction of overhanging features due to inherent support material, certain geometric complexities and functionalities are lost, making this technology less suitable for structural parts. One promising technique which aims facilitate this is DED. Whilst currently gaining considerable traction among industrial manufacturers; DED remains in the infancy of the development stage. Although capable of building components in continuous freeform for structural use, it has predominantly been used for spot repairs because manufacturing speeds of this method simply cannot compete with traditional manufacturing techniques at this time.

In contrast to the difficulties of 3D printing with purely metal or ceramic compounds, the AM industry has made vast use of light weight polymers for rapid prototyping applications. Whether a room temperature liquid resin or thermoplastics with extremely low melting points (relative to metals/ceramics), the low costs for bulk materials and flexible nature of plastic processability are major contributing factors to the adoption of this class of material throughout the history of AM [28]. Some common thermoplastics used in the FDM process include:

acrylonitrile butadiene styrene (ABS); nylon 12; polylactic acid (PLA); and thermoplastic polyurethane (TPU), the material that most smartphone cases are made of [29]. Both thermoplastics as well as thermosetting polymers, epoxy resins for example, can be processed by 3D printing technology [30]. Despite the potential for complex geometric structures, polymer products as a class lack the desired mechanical strengths and functionalities for end-use industrial applications – a commonality amongst most components produced by 3D printing techniques [11].

While various AM techniques have the capability to print components from pure materials, these methods often restrict the components to a single class of material, mono-functionality, and/or significant post-processing requirements as a result of the available mainstream technologies [31]. Drawing out specifically desirable properties from each of the material classes and imparting them into a single component through some combination thereof is one notable solution [11]. These types of material combinations are the basic principle behind composite materials.

1.4.2 Role of Composites in AM

Developing advanced composite materials for 3D printing has the potential to drastically reduce many pitfalls, such as post-processing costs, faced when applying AM techniques to pure materials. The vast majority of peer reviewed articles and publications in this field have focused on furthering development of processing techniques or improvements to pure polymer manufacturing for FDM commercialization over the past thirty years. However, developments of thermoplastic composites for AM has seen a recent uptick in academic interest [32]. While the research interest for developing composites materials for this application space is quite new, some limited examples are available [33]–[35].

Due to their low cost, ceramic or metal powders are common reinforcements for polymer matrix composites. With a compatible processability of polymers and micron-sized particles, particle reinforced composites offer a good avenue for pairing favorable properties of the parent materials [25]. Strategic improvements commonly sought after from particle reinforced composites in AM include “improved tensile/storage modulus by adding glass beads [36], iron or copper particles [37], improved wear resistance by adding aluminum and

aluminum oxide(Al2O3) [38], and improved dielectric permittivity by adding ceramic [39], [40] or tungsten [41] particles." Masood and Song [42], Venables [43], Nikzad et al. [37],[44] published work describing the development of some metal/polymer (thermoplastic) composites for use in an FDM printer. The aim in each of these investigations was to reinforce nylon and FDM-grade ABS with iron particles; achieving a printable filaments of 70/30% (nylon/iron) [42], 60/40% (nylon/iron) [43], and 90/10% (ABS/iron) respectively [44].

Despite recent interest and developments for polymer composites within the AM community, they remain broadly unaccepted by most industries. X. Wang et al. [11] identify and detail three major limitations to be overcome before adoption of 3D printed composite materials will be widely accepted:

- Material Availability – "The wide application of 3D printing is severely limited by printable materials. Currently, only thermoplastic polymer with low glass transition temperature and suitable melting viscosity, powder formed materials and a few photopolymers could be used in 3D printing. However, these limited materials could not meet the variety [of] requirements of industry application[s] and thus the diversity of materials must increase. Synthesis of matrix materials with special properties, discover[y] of new reinforcement and discover[y] of suitable mixing composition are critical to increase the versatility of composites printing technology. Sustainable materials are also promising to be developed to reduce material cost and environmental impact."
- Material Performance – "Although reinforcement helps improve the performance of polymer composites, compared with polymer composites manufactured by traditional molding methods, most of the printed composites still have low mechanical strength and are not able to meet the functional requirement. Therefore, additional post-treatment steps involving infiltration or consolidation have been used to improve the performance of printed products. However, these steps further increase the cost and processing time. A main reason for the low mechanical strength is the presence of voids in printed parts. The addition of reinforcement may further increase the porosity due to the poor interfacial bonding with matrix. Therefore, the improvement brought by reinforcement may be compensated by the induced porosity. How to eliminate the

formation of void[s] during printing and ensure good interfacial bonding between matrix and reinforcement requires further significant research. Moreover, the repeatability and consistency of manufactured parts cannot be guaranteed by printing, thus approaches to ensure the uniform properties of printed parts need to be investigated in depth."

- Scalability and Machine Controls – "Most printing processes are time-consuming now, and it is difficult to fabricate parts that have large volume. These inhibit their industry adoption. New printing techniques based on scalable and fast processing of materials should be developed. For example, digital light processing is an efficient improvement of SLA process. A layer of photopolymer is fabricated during one-time projection, which greatly reduces the processing time. Similar improvement should be done for other techniques. Another area of growth centers on the need for feedback systems. If an error occurs during printing now, the process needs to be suspended, which causes the waste of time and materials. Feedback systems should be built in the printer to have a response to the process change. Additional progress for 3D printers is to increase the printing resolution without extending printing time or sacrificing geometry complexity of products."

1.5 Manufacturing Space Contribution

In relation to the subjects of discussion thus far, this work falls under the domain which consists of material extrusion AM techniques applied to composite materials. More specifically, the proceeding work focuses on the machine control of a micro-Robotic Deposition system (μRD) for printing thermosetting ferrous-polymer composite materials with applications for rapid manufacturing of magnetically functional components.

1.6 Thesis Chapter Outline

This thesis is organized in the following way: First, the overview of manufacturing techniques was presented above. This overview heavily concentrated on the space of manufacturing that is additive by nature. Chapter 1 further detailed the types and roles of

different materials in the AM domains. Chapter 2 contains some background information on magnetic components (specifically the cores) in power electronics and the problem motivating this work. This chapter also gives an outline of the solutions presented in detail through Chapters 3-5.

The third chapter contains information and recipes on the analog material system used in this work. In Chapter 4 the reader will find information on the physical elements of the electromechanical system (the μRD) facilitating the additive manufacturing aspects of this thesis. Chapter 5 is a discussion on the development of the machine control implemented on the μRD system. Results for the ink materials and machine control developed through the previous chapters is given in Chapter 6 for additively manufacturing ferromagnetic cores. Finally, Chapter 7 makes some concluding remarks on the work presented and discusses some potential direction for future work relating to this thesis.

Chapter 2
Motivating Problem

Technology continues to accelerate through the 21st century with a growing demand for miniaturization of electronic systems and increased energy efficiency from existing power supplies [45]–[47]. Increasing the power density of high-frequency switching and pulsed-power energy modules of these electrical power systems face a significant challenge in the form of magnetic core losses. Developing new low/lossless magnetic materials is essential to increasing the efficiency of power electronics [48]. It is common for magnetic components such as inductors and transformers to occupy the largest volume and mass fractions of power electronics systems [45], [47], [49]–[51]. In recent years, these components have seen significantly less improvements compared to the remainder of the circuit components, with respect to power density. This, despite being considered the "workhorse of power systems" and the disproportionate representation on the circuit [45], [47]. A major limiting factor to improving the efficiency/ power density capabilities of magnetic components is the temperature increase experienced during operation [52]. These thermal issues contribute to power loss and are directly associated with the magnetic cores found in most inductors and transformers, referred to as core losses [46].

Furthermore, the methods of fabrication and integration for these components must be addressed to meet the requirements of these new materials and technological trends [51].Current methods of integration for these magnetic components require several intricate and laborious steps including some at extreme temperatures [53]. These extreme temperatures can limit the ability of manufacturers to directly integrate the fabrication steps of magnetic components and power modules.

This chapter gives a brief background to the material and fabrication problems. Potential solutions from the fields of nanomaterials science and additive manufacturing are offered as the target of the work presented in the following chapters. Superparamagnetic iron nanoparticles have been shown to be a useful solution in applications such as drug delivery and biomedical imaging and are the materials solution addressed in this work. Due to the chemistry involved during the synthesis and stabilization of these nanoparticles (specifics of which are not addressed by this author), a material extrusion AM technique is chosen and presented as the potential fabrication solution.

2.1 Core Losses

When running AC current through electro-magnetic devices such as inductors and transformers, the windings produce an alternating magnetic field with an associated magnetizing flux. While ferromagnetic cores greatly improve the overall power and efficiencies in these devices, there are drawbacks associated with the alternating magnetization of the cores called core losses. There are two main physical phenomena that make up core losses: hysteresis losses and eddy current losses [54]. Both phenomena are dissipated in the form of heat, contributing to energy wasted and increased thermal loads during operation of electronics systems.

2.1.1 Hysteresis Losses

Ferromagnetic materials are made up of collections of several, smaller particles containing magnetic domains of randomly oriented dipoles separated by domain walls. These domains are sensitive to the flux of external electromagnetic fields (EMF) such as those produced by current flowing through the windings of an inductor. When these domains come in contact with an EMF, the dipoles of the domains align themselves in the direction of the external field by movement of the domain walls [54]. The energy spent moving these domains walls when realigning the dipoles under AC current is called hysteresis loss and is dissipated as heat.

Hysteresis loss can be thought of as a material's resistance to change in the magnetic direction of an externally applied field, or magnetically induced friction within the core

material. The total energy lost can be measured by the area contained in the enveloping hysteresis loop for a B-H loop as in Figure 2.2.

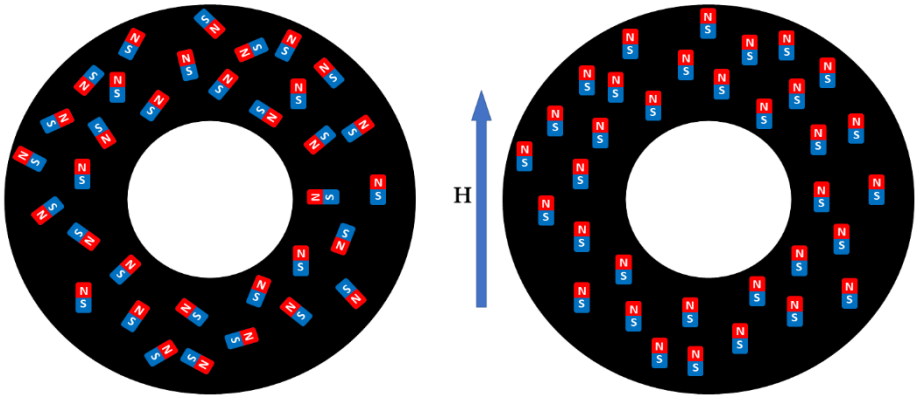

Figure 2.1 Depiction of randomly oriented magnetic domains/dipoles under zero field (left) and magnetic domains being aligned with an external EMF (right).

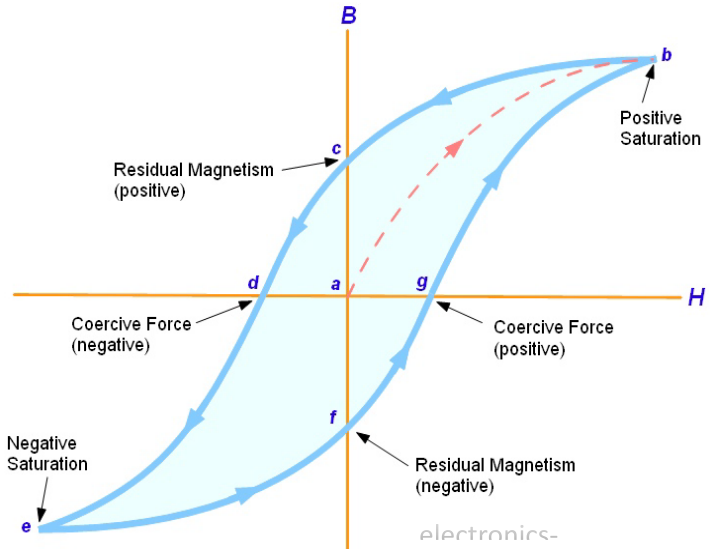

Figure 2.2 Typical hysteresis loop of a magnetic core: b, e) point in the BH curve where the core reaches magnetic saturation; c, f) the remnant or residual magnetization in the core after removing the external field; d, g) the coercive forces needed to remove the residual magnetization of the core from an applied field in the opposite direction. Magnetic susceptibility χ can be taken as the slope of the BH response during the initial magnetization at (a)

2.1.2 Eddy Current Losses

When current is run through a conductor it generates an electromagnetic field. When this field comes in contact with another conductive element it induces additional circulating currents within it called eddy currents. Magnetic cores are constructed of predominantly conductive materials, making them susceptible to such eddy currents. These eddy currents flow in opposition to the supplied current, generating heat. The heat energy generated from these eddy currents is what makes up the eddy current losses of magnetic cores. The magnitude of induced current within a core is inversely related to its resistivity.

One method of reducing eddy currents is to then shrink the affected cross-sectional area of the core. This is done by stacking laminated sheets of core material or binding insulated sections of the core together. By using powdered magnetic materials held together by sintering or nonconductive binder materials the affected areas – and subsequent eddy currents – can be reduced further. Figure 2.3 depicts this phenomenon as well as a progression from (left to right) a solid core to laminated sections to insulated powder core material, reducing the eddy current presence in the core.

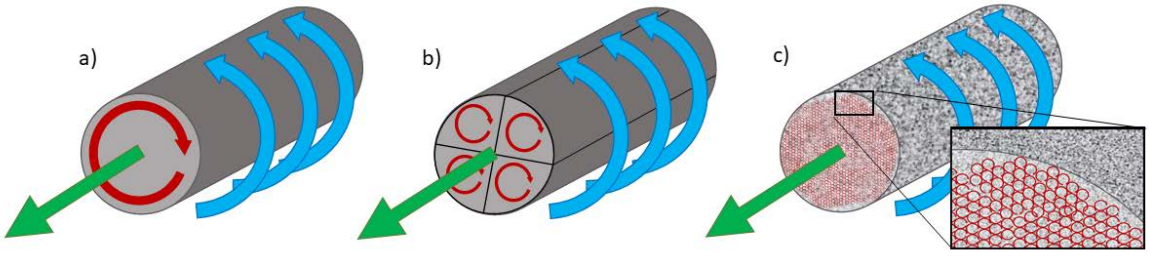

Figure 2.3 Blue arrows indicate the flow of current. Green arrow(s) indicate direction and magnitude of the induced EMF. Red arrow(s) indicate direction and magnitude of eddy currents induced by the EMF. a) Depicts the large eddy current moment created in a bulk piece of uninsulated core, b) depicts eddy current moments being reduced from (a) by insulating multiple sections of a core, c) depicts a powdered core with several smaller eddy currents which sum to a lesser overall moment than those in (a) or (b).

2.2 Fabrication of Soft-magnetic Cores

Traditional materials for creating soft-magnetic cores include using small-grain, ferromagnetic, metal powders. Examples of these include iron-oxides such as magnetite and magnesium, zinc, nickel or cobalt containing ferrous-metallic oxides. Conventional fabrication methods for this class of soft-magnetic cores have traditionally been either high-pressure powder compaction or powder injection molding, both of which require post processing by high temperature sintering (900 to 2000 $°C$) [49], [50], [55].

The temperatures required under these techniques render neither as desirable for direct component integration with the power electronics manufacturing nor retention of the desirable magnetic properties. For example, sintering of iron powder at high temperatures is known to create larger magnetic domains within a component thereby allowing for increased eddy current losses during operation as compared to the idealized grain size of the original powder.

These thermal issues are even more detrimental if using – very combustible – iron nanoparticles. Use of X-oxide nanoparticles can mitigate this risk factor. However, there still exists the tendency for nanoparticles to clump together making larger particles called agglomeration. Agglomeration is a difficult phenomenon to avoid at low temps, and nearly impossible at sintering temperatures. Therefore, cores that are comprised of highly electrical resistive material which could separate the individual particles of magnetic powder while processible at relatively low temperatures - far lower than required by sintering – are of particular interest for high-power systems [56], [57].

2.3 Potential Solutions

2.3.1 Desired Magnetic Core Properties

Core losses experienced by magnetic components can vary greatly based on the materials that make up the core. Fujita et al. [46] provide the minimal requirements for magnetic cores used in high-frequency applications as soft magnetism, and low losses. However, a stricter set of desirable properties for improved power density can be found in [47]. These include high saturation magnetization (M_{sat}), relative permeability μ_r , and electrical

resistivity (to avoid eddy current losses). By combining high M_{sat} values with a flat permeability response up to several MHz, losses can be greatly reduced compared to standard materials available [58]. Many high-frequency applications utilize soft-magnetic materials to mitigate some of these losses [52], [59]–[61]. Soft-magnetic materials are those which exhibit low magnetic coercivity making them easily magnetized and demagnetized with an external field, generally producing lower hysteresis [55], [62], [63]. Soft-ferrite magnetic materials are one avenue that is commonly explored in industry to address the minimal requirements mentioned by Fujita et al. However, iron and iron-oxide nanoparticles that achieve superparamagnetic properties can address the stronger requirements needed for increased power density.

2.3.2 Proposed Nanomaterial Solution

The domain types and magnetic properties for ferromagnets can change drastically as the particle size decreases. A critical diameter, D_C, defines the separation of particles into single and multidomain regions, see Figure 2.4. This critical size is often in the tens of nanometers in length. For particles of size $> D_C$ there are multiple randomly oriented magnetic domains within an individual particle, separated by domain walls. For particles of size $< D_C$ there is a single stable magnetic domain per particle. Generally, both single and multidomain particles exhibit ferromagnetic properties such as low coercivity (compared to hard magnets) and moderate to high residual magnetism. When the particles are small enough ($< D_{SP} \approx$ 40-60nm) they become superparamagnetic.

Superparamagnetism occurs only in these sufficiently small particles. It is signified by the physical phenomenon of a single, giant magnetic moment randomly flipping orientation under certain thermal conditions [47], [65]. This random flipping of magnetic moments leads to an average net zero magnetization in the absence of external fields. This means that under superparamagnetic conditions, particles exhibit no coercivity or residual magnetization from removing an external field while retaining the magnetic saturation potential of larger particles. Superparamagnetic materials then, by definition, have no hysteresis under alternating current. Furthermore, at sizes sufficient for superparamagnetism, they will not be large enough to

support intraparticle eddy currents [47]; thereby completely eliminating the major contributions to core loss in magnetic components.

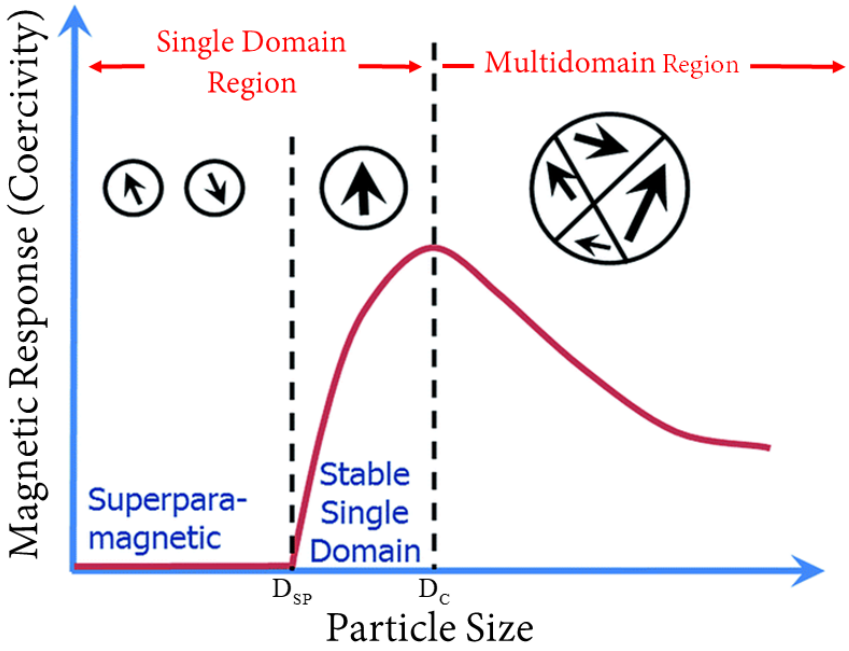

Figure 2.4 Scheme of particle size dependent magnetic domain properties (image derived from [64])

2.3.3 AM Solution to Fabrication

To avoid the ill-effects of high temperature and pressure manufacturing of ferrite cores, this work proposes a material extrusion type AM solution. Material extrusion offers the greatest versatility in choice of material systems which allows for iterating through specific chemistries of composite material easily. AM also offers the chance to investigate more novel form factors than those available through molded geometries.

2.3.4 Analog Material Choice for Feasibility

Nanoparticle development and synthesis are extremely costly both financially and in time. Hence, a cheaper and more easily obtained material is chosen as an analog substitute for the SPNP's in this initial work. This allows for proper setup and testing of the AM system to produce components of a similar material system without wasting valuable product. Carbonyl

iron is a high-purity form of small grain (~5μm) iron powder. This ferrite material is “used extensively as powder core [material] for inductor applications in high-power circuits” [47]. And has shown similar retention of magnetic susceptibility to that of iron nanoparticles (Figure 2.5).

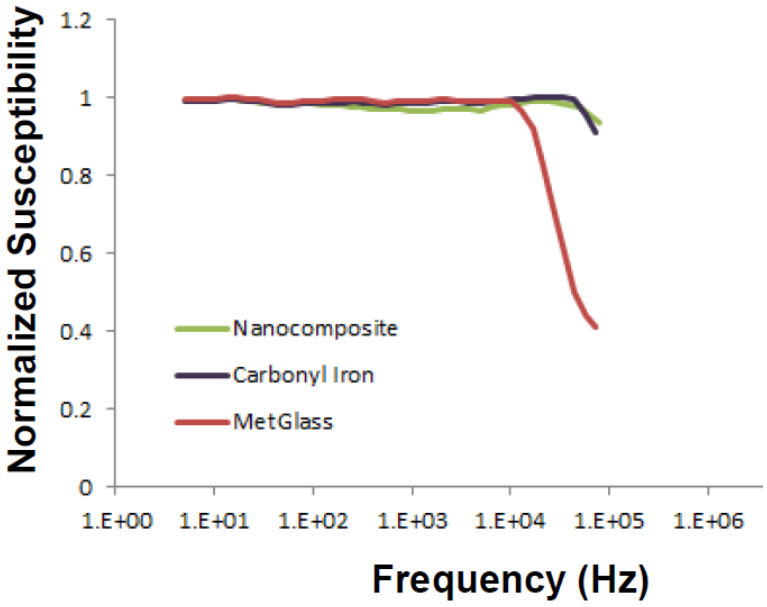

Figure 2.5 Comparison of magnetic susceptibility in iron nanocomposite, carbonyl iron particles, and a leading amorphous material (MetGlass) up to 100 kHz

Several works have utilized epoxy, silicon, phosphate, SiO2, and Al2O3 [66]–[69] as insulating materials to improve the magnetic properties of powder cores. Epoxy resins are a class of polymer that are used extensively in the adhesives and coatings industry. These polymer matrices have recently seen growing interest in applications to additive manufacturing of composite materials [70], [71]. Sugawa et al. [72] recently created carbonyl iron-epoxy magnetic cores for high-current magnetic components fabricated directly into a system. They showed that using the epoxy matrix imparted sufficient dispersion of the iron powder leading to lower losses at high frequencies. This work utilizes this insight to argue that a similar composite is a sufficient analog to iron/ iron-oxide nanocomposites for testing and set up of a material extrusion AM system to fabricate more complex topologies of magnetic cores.

Chapter 3
Material System

Material Extrusion offers a diverse range of material systems to use for printing. This work builds off previous efforts that focus specifically on the intersection of precision control of machines and material systems. Previously developed inks in this focus area were based on colloidal sciences of high solids loading ceramic slurries. These previous works utilized hydroxyapatite (HA) inks to investigate printing of bone scaffold materials [10, 11]. Research efforts in other domains have developed similar colloidal inks [9], polyelectrolyte inks, and fiber reinforced epoxy composite inks compatible with this type of 3D printing scheme, though much of the research efforts of the past focus on colloidal suspensions and slurries. This chapter will discuss the various properties needed for an ink to be printed under uRD as well as the functional characteristics desired for use in systems presented in Chapter 2. Subsequent discussion on the choice of an epoxy material system, specific formulation and procedures for the ferromagnetic ink and examples are given.

3.1 Ink Properties

The aim of this study is to create magnetically functional, rather than simply structural, components. With that, there are the typically required properties necessary for material extrusion and printing along with additionally imposed functional properties of the final part. Both must be leveraged and addressed for successful fabrication.

3.1.1 Properties Necessary for AM

Inks must be able to flow from a deposition nozzle under moderate to high shearing; yet settle in its deposited cylindrical shape almost immediately in order to retain the desired component feature topologies. Material systems must further exhibit a stiffness such that, when deposited, each i^{th} -layer is capable of supporting the weight of the $n-i$ remaining layers whilst retaining the originally deposited morphology, where n is the total number of layers needed for the printed component. Some advanced inks designed for structural purposes also impose a requirement that the filament paths must be able to span some specified gap distance without sagging or deflection [9]. This work will investigate components that have 100 percent infills and no gapping sections which eliminates this last requirement as a required property to achieve/investigate. The rheological flow type that best fits these conditions is a non-Newtonian pseudoplastic behavior. As seen in Fig 3.1 this describes a shear-thinning property in which the material viscosity decreases with an increase in applied shear rate and recovers the static viscosity as the shearing is removed.

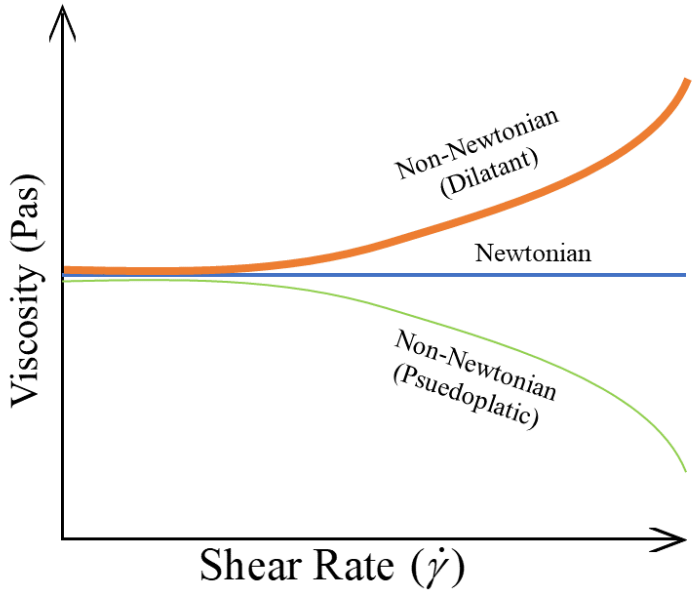

Figure 3.1 Rheological flows for Shear Rate vs. Viscosity

3.1.2 Functional Properties

Beyond the basic rheological properties needed for extrusion/ printability, the ink system developed in this project has functional ferromagnetic requirements put on it. Detailed in Chapter 2, we aim to impart the fabricated parts with high magnetic susceptibility (or equivalently permeability), high saturation magnetization, and low hysteresis to mimic as close to possible the properties of the Iron nanoparticles under development at Sandia National Laboratory.

3.1.3 Additional Properties

As an additional consideration to future researchers, this project aims to develop a widely accessible, easily synthesized, and relatively cheap ink system that does not require fabricated parts to go through post-processing operations such as high temperature annealing. Specifically, we require that the ink solidify under standard ambient conditions in under 4 hours so that components may go from ink to part within the same business day window.

3.2 Proposed Analog Material Solution

The material system for this work is an initial effort to determine the efficacy of dense ferrous composites in the fabrication of components through a material extrusion-based AM technique. For this purpose, well established materials were selected. The backbone for the proposed material system will rely on a thermosetting polymer matrix. Thermosets are a class of polymer that are characterized by their irreversible monomer crosslinking reactions (called curing) resulting in solid three-dimensional parts that cannot be melted down and reprocessed. Epoxies are a subclass of such thermosetting polymers which often require a chemical additive such as an amine group, to catalyze the crosslinking process. Epoxies are a great choice for printable ink matrices because of their easily tunable properties through proper choice of filler materials and appropriate catalyst or hardening agent. Bisyphenol-A Dyglycidylether (DGEBA) is the most commonly used industrial epoxy throughout the world and is the epoxy of choice in this work. To address our room temperature and fast curing goals, the author chose

to employ Diethylenetriamine (DETA) as the catalyst compound to complement the DGEBA resin.

To address the magnetic characteristics desired of the core material, this project used a high-purity iron powder called carbonyl iron. With the appropriate particle sizing, this provides an analog for the future use of nanoparticles under development at SNL, achieving magnetic characteristics near those outlined in Chapter 2.

Imparting the epoxy matrix with the rheological properties need for printing via uRD is accomplished through the addition of fumed silica. Relatively low amounts of fumed silica nanoparticles (1-10 wt%) are known to impart thixotropic or pseudoplastic shearing behaviors in polymer composites and aqueous gel suspensions [2, 3]. An additionally beneficial property of fumed silica is its extremely high surface area. This allows the silica particles to act as dispersal units for the iron particles within the epoxy matrix, minimizing interparticle eddy currents further and acting as another analog to the surfactants used currently by SNL to stabilize the iron nanoparticles from agglomerating.

3.3 Ferromagnetic Ink Synthesis

3.3.1 Materials Used

The ferromagnetic ink used in these proceedings is a thermosetting epoxy matrix composite. The epoxy system used is the monomer resin Bisphenol-A diglycidyl ether (BADGE or DGEBA depending on the author) and the hardening agent Diethelyne Triamine (DETA). This epoxy matrix is a fairly well-studied system for room temperature cures and adequate polymer hardness. A powdered carbonyl iron is added to obtain the desired ferromagnetic properties. Fumed silica powder is used to tune the needed rheological properties. Carbonyl iron is 99.5% pure iron powder with an spherical particle size ranging from 5-9 um provided by Sigma Aldrich, CAS# 7439-89-6. The fumed silica glass is a nanosized glass powder provided by Sigma, CAS# 112945-52-5, which has an average particle size of roughly 10nm resulting in variably sized chains of 10-30 aglomerated units or 0.1-0.3 um long chains of spheres.

3.3.2 Stoichiometric Quantities

To create the ferromagnetic inks used in this work, 5.56 grams of DGEBA are used to every 20 grams of carbonyl iron. The stochiometric amount of DETA used to cure DGEAB is 11-14 parts per hundred (phr) of neat resin resulting in 612-778 mg of hardener in this case. This work used 685 ± 20 mg for the inks, roughly 12-12.5 phr. The amount of dispersant, fumed silica nanoparticles, used was 385 mg.

3.3.3 Ink Synthesis Procedure

Making sure DGEBA is in its liquid form, add 5.56 grams to an appropriately sized mixing cup. Should the resin show signs of crystallization, heat to 42-45 degrees Celsius to return it to a liquid state. This can occur in slightly cooler rooms as the melting point is near room temperature. Carefully add carbonyl iron in small amounts to the mixing cup until 20 grams is achieved. Allow the iron powder to wet for approximately 5 minutes before adding fumed silica nanoparticles. Once again, the user should add in small amounts or batches until the correct amount is obtained. Thoroughly mix the composite resin by hand using a wooden tongue depressor or other stir rod for 3-4 minutes or until sufficiently homogenized.

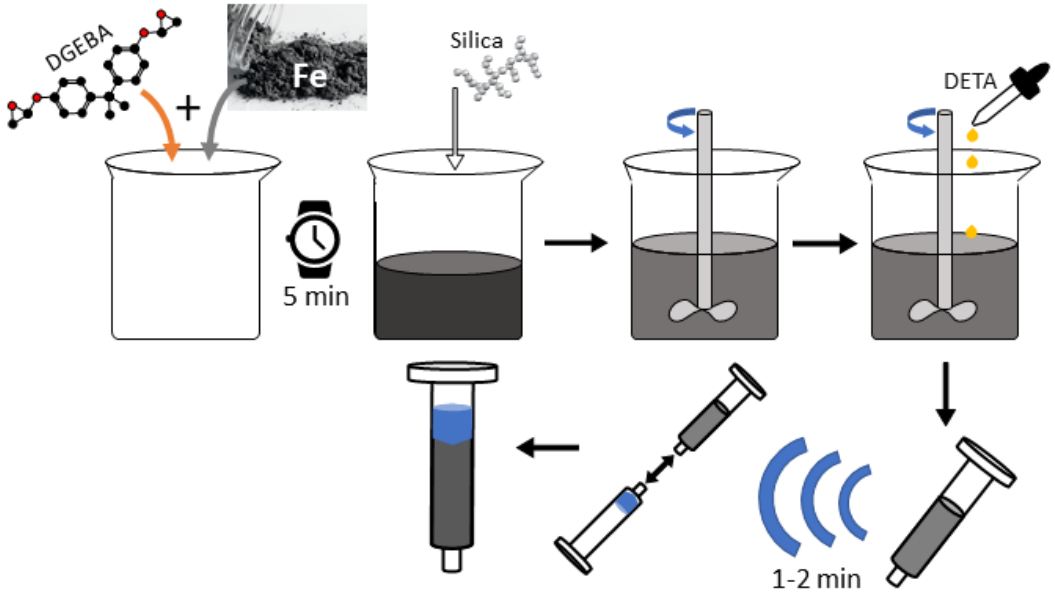

Figure 3.2 Flow chart of the ink synthesis procedure described in section 3.3.6. Carbonyl Iron Powder image derived from BASF brochure [8].

An alternative method for homogenization is to use a planetary centrifugal mixer such as those available from Thinky. If using this method, one can mix the constituents above for as little as 1 minute to achieve proper homogenization. One can refer to the Thinky web page [7] for further information on devices and procedures of operation for this method. Users will observe that in the latter method, the composite resin will heat up dramatically from the high rpm mixing involved; in which case, allow the resin to cool to room temperature before adding the hardener. This will avoid any undesired exothermic runaway from occurring which would result in a failed or rapidly cured ink before printing can take place.

In its above state (DGEBA + Fe + Si), the ink was seen to be viable for up to a week in ambient conditions when stored and sealed properly. Storage for longer periods may be possible but was not the aim of this investigation nor is suggested. Correct rheology can be observed when the composite ink is able to retain small peaks and/or hold to a stirring stick when upside down as seen in Fig 3.3.

Figure 3.3 Correct rheology of final composite with small peaks holding shape

When the user is ready to print the ink, add the correct amount of hardener DETA to the room temperature resin composite and quickly begin mixing the hardener in to the system by hand for no more than 1 minute. Allow the ink to sit for 1-2 minutes while prepping the next steps. Using a Luer lock style syringe, insert the accompanying piston as far as possible

within the chamber and attach the syringe-syringe transfer device to the nozzle end. This is the reservoir to be used during the printing.

Ink loading first takes place in another Luer style syringe designated as the transfer syringe to reduce voids or bubbles during the extrusion process. Cap the nozzle end of the transfer syringe and begin filling the transfer syringe with ink, tapping the syringe against a hard surface between scoops to remove any visibly large pockets of air. Once filled, use a shaking/vibrating stage device such as a common shake plate for 1-2 minutes – to release any smaller air pockets. After appropriate agitation, insert a correctly sized plunger to the transfer syringe and attach the reservoir syringe via the transfer coupler. Smoothly and slowly transfer the ink to the reservoir. Finally, load the reservoir syringe on to the extrusion system by screwing the reservoir on to the feed path and attaching the pneumatic tubing.

Chapter 4
Robotic System Design

In 1998, the Alleyne Research Lab at the University of Illinois acquired the Motorola XYZ Mylar Robot, now known as the micro-Robotic Deposition (μRD) System. Initially utilized for circuit board manufacturing by the Motorola Corporation, previous researchers disassembled much of the original pick-and-place machinery and retrofitted its XYZ stages with μRD capabilities [73]. The vast majority of these retrofits took place over the following decade and lasted until roughly 2015 when many of new systems either ran into software compatibility and update issues or general disrepair [74]. This thesis aims to briefly discuss some of the retrofits of the past as well as the current strategies employed with this latest μRD retrofit.

As mentioned in Chapter 1, μRD is a material extrusion form of AM where carefully tailored colloidal inks are deposited to a given substrate in pre-determined paths to create three-dimensional parts [75] as shown in Figure 4.1. Outlined in [75], "μRD systems have four main components: 1) the material system or the colloidal ink, 2) the substrate, 3) the positioning system, and 4) the extrusion system." The following sections discuss the past and present iterations of components 2-4. The material system and ink development are subjects discussed in Chapter 3.

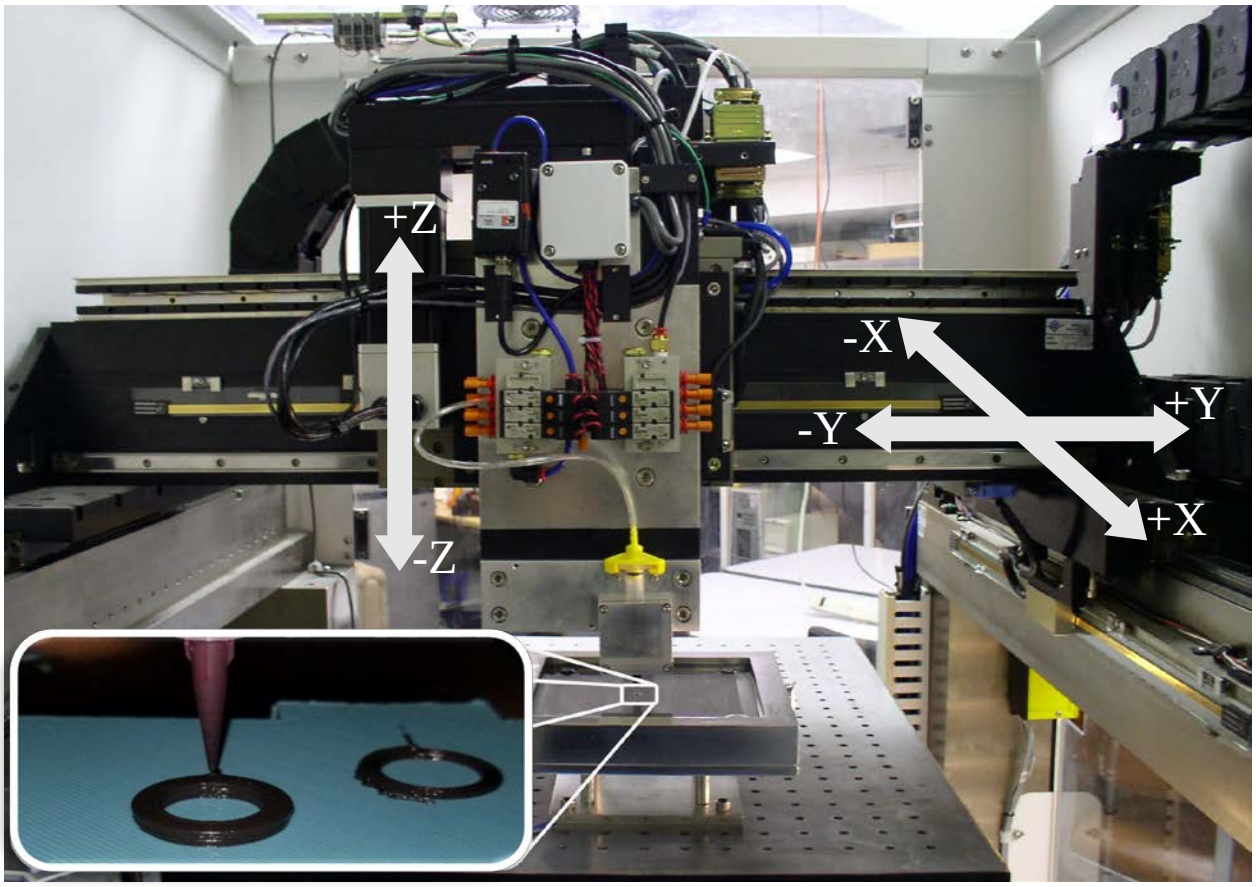

Figure 4.1 µRD System [76]

4.1 Substrate

The substrate for a μRD system has just two traditional requirements; namely, it must be a flat, solid material and it must not be reactive with the chemistry of the material system used in the ink [75].

Previous deposition procedures would extrude hydroxyapatite lattices on a small aluminum plate. This plate was coated with a black paint for contrast and a light adhesive before submersion in an oil bath constructed of machined aluminum. A pneumatically controlled passive vibration isolation table – Benchmate 2214 – automatically levels the bath via mechanical valves. A larger aluminum stage is used to support the Benchmate and substrate and once supported accompanying lights and cameras used by previous researchers in our lab

for magnifying the deposition area to a nearby monitor. Several issues with the existing camera and lighting elements in the last five years lead to these systems being left out of the most recent build.

4.1.1 Recent Modifications

In this work a top cover has been added atop the existing aluminum bath. The cover is machined from 6021 aluminum to affix to the edges of the bath with a tolerance of 0.05 inches. The cover has a 4” by 4” square inset 0.5 inches at its center which supports the new substrate. The new substrate is a flat silicone mold with dimensions 4x4x0.625 inches shown in Fig 4.2. This author found that the silicone substrate is preferential to metallic, ceramic or glass substrates presumably because of the epoxy nature of the ink system. The silicone allows for the easiest removal of cured samples without destruction or etching of the substrate.

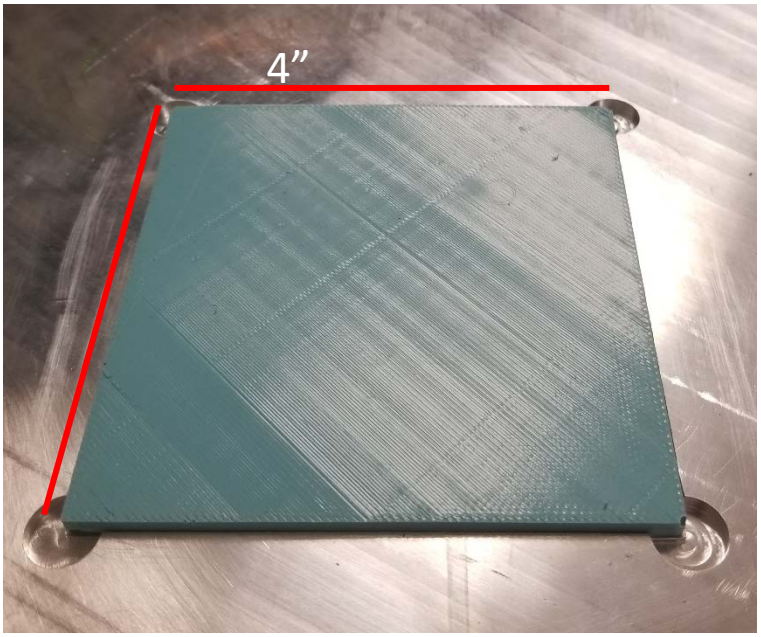

Figure 4.2 Silicone printing substrate. Substrate is formed from PLA molds that were 3D printed using a Lulzbot TAZ6 at the University of Illinois, Urbana-Champaign’s Innovation Studio

4.2 XYZ Positioning System

The XYZ positioning system is comprised of the XY gantry stage and the Z-axis. The XY stage is an Aerotech AGS10500-500 Linear Motor Gantry. For this stage, the X-axis carries the Y-axis in an H-drive configuration, driven by an Aerotech BLM-325 and BLM-264 linear motor, respectively. The Z-axis is a precision ballscrew stage mounted to the Y-Axis and is driven by an Aerotech BM130 rotary motor via a timing belt and gearbox. Fig 4.1 depicts the positioning stages and orientation of the μRD.

Each axis is equipped with Reinshaw linear optical encoders, shown in Fig 4.4, for positional feedback with a resolution of 1 μm. Three Aerotech BA30 Servo Amplifiers power the individual axes of the μRD. The XYZ positioning system has been retrofitted with the Aerotech Nservo multi-axis servo controller shown in Figure 4.5. The Nservo allows for compatible computer software(s) to interact with the analog servo amps, allowing for closed loop control of position and velocity commands to the XYZ stages of the system.

Figure 4.3 Renishaw linear optical encoders installed on the X (left) and Z-Axes (right). The same encoder model is used for X and Y.

Figure 4.4 Aerotech's Nservo multi-axis servo controller [5, 6]

4.3 Extrusion system

Extrusion systems for μRD typically fall into one of two categories; 1) controlled pressure, or 2) controlled displacement [79]. Previous efforts have implemented both extrusion techniques with the μRD in the past [1, 3]. Implementation of the controlled pressure extrusion technique utilized a syringe and piston assembly as the ink reservoir. An onboard pneumatic system connected to the computer interface controlled the delivery of specified amounts of pressure at the piston to extrude the ink [73]. Controlled pressure systems are ideal for those with nozzle diameters smaller than 100 μm because "a mechanical system cannot produce the fine displacement resolutions required to continuously extrude the ink" [75].

However, the controlled displacement extrusion technique is the most suitable for systems with nozzle diameters in the 100 μm – 1 mm range "because the controlled pressure method is more sensitive to slight variations in ink rheology" [79]. Controlled displacement extrusion is a mechanical system in which displacement of a plunger or other mechanical system is controlled to extrude the ink. A multi-material deposition system was built using the controlled displacement approach, replacing the original controlled pressure system. Each of

the four extruders used a lead screw assembly and motor/encoder combination to control the displacement of the plunger/piston, therein providing the necessary chamber pressure for extrusion. Various issues in this multi-material system arose in the years since its implementation; which are more thoroughly outlined in [74]. A brief list of issues is given:

- The machined syringe walls began to deteriorate and etch
- Additional friction along syringe walls overworked extruder motors
- Control of transient ink flow behavior became excessively difficult
- Uncontrolled material flow would lead to inconsistent printed parts.

4.3.1 Auger Valve Extrusion System

The current method for deposition is a hybrid of the two traditional extrusion strategies mentioned above called a rotary screw valve system – or auger valve extruder.

4.3.1.1 Brief Theory of Operation

Auger valves operate under the basic theory that dictates archimedean screws. The material is delivered from the source reservoir or feedstock to the desired location by physical turning of a threaded screw within a hollowed cylinder as shown in Fig 4.6. The shearing force created by the turning of the screw forces the material through a feed chamber between threads. In this case, the feed chamber and screw determine the amount of material extruded independent from the pressure at the reservoir and the viscosity of the ink.

Auger valves are a staple in plastic circuit board (PCB) manufacturing for depositing size-controlled beads of solder paste or small lines of adhesive between parts. Solder paste is another thixotropic composite material which is made up of a matrix blend of flux and adhesive filled with a conductive powder such as a silver or tin alloy. The similarity in material composition and rheology of the ink system used for this project to that of general solder pastes, and wide use within industry, lend credit to the auger valve as an ideal candidate for our extrusion system.

A simplified formula for the extruded path rate L (mm/s) from the nozzle of an auger valve type extrusion system can be given by the following equation:

$$L = \frac{hpv}{15\pi d^2}\sqrt{R^2 + (\pi D)^2} \tag{4.1}$$

Where d is the inner diameter of the nozzle, v is the speed of the auger screw in rpm, D is the diameter of the feed chamber, R is the radius of the feed screw, r is the radius of the main shaft, $h = R - r$ is the depth of the threads, p is the pitch of the feed screw.

4.3.1.2 Technical Specifications

The current system in place is the Techcon Auger Valve TS7000-DMP shown in Fig 4.7. The auger system utilizes a pressurized syringe to feed material into a feed chamber. The feed chamber contains a threaded screw which is operated by a 6-Watt DC brushless motor. By applying the appropriate power, the DC motor rotates the feed screw counter-clockwise (clockwise) resulting in extruded (retracted) material at the nozzle tip. In theory, the auger valve serves to more precisely meter the material flowrate than either controlled pressure or previous displacement driven μRD applications.

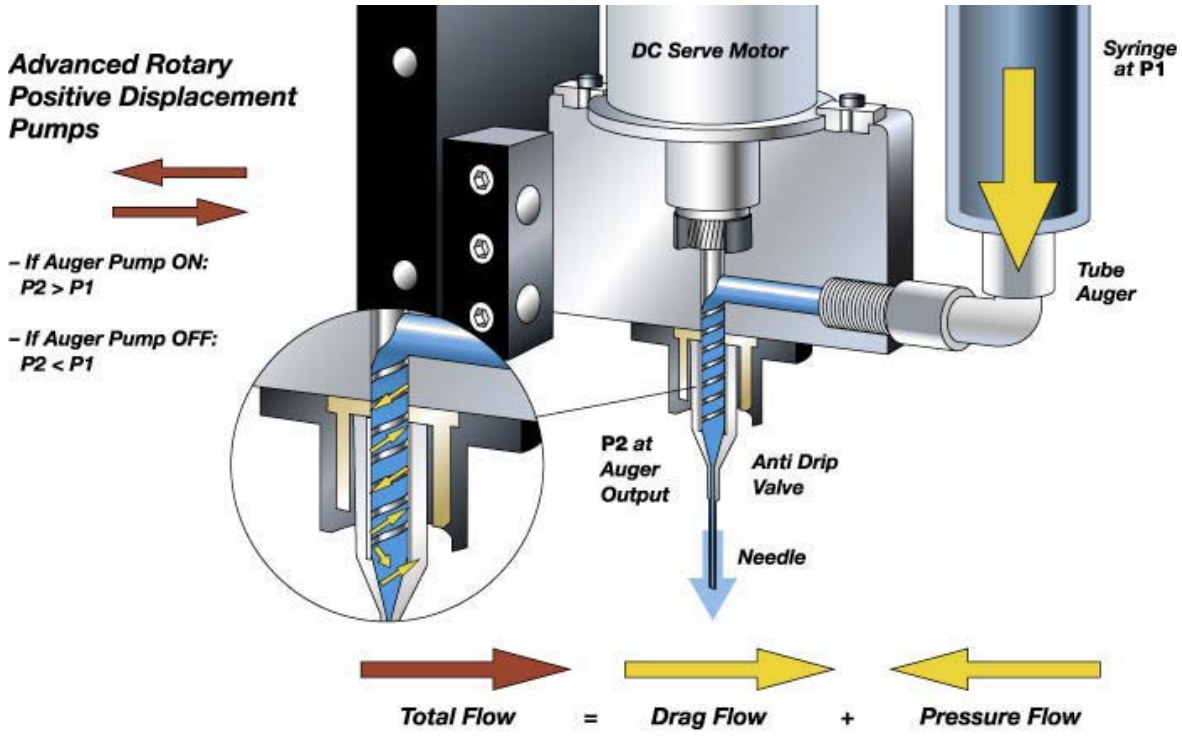

Figure 4.5 Depiction of an auger valve extrusion system [80]

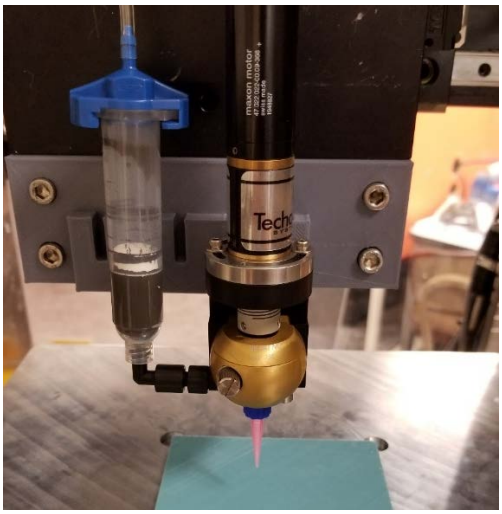

Figure 4.6 Techcon's auger valve integrated with the μRD system

The Techcon Auger system is designed to work with a disposable feed path assembly which houses the feeder screw and has Luer lock style attachments at either end for compatible syringe reservoirs and nozzle tips. This separates the ink system from the motor and gearbox, preventing clogging or damage to the crucial parts of the mechanical system. The feeder screws chosen for this work are a pitch of 8 to reduce shearing and unwanted residual heat into the ink system.

The syringe reservoirs are provided by Nordson EFD and can range from 3-10 cc depending on volumes need for the specific part being fabricated. Pressure to the reservoir is supplied by a constant wall supply of compressed air which is regulated down to ~30 psi by a manual pressure regulator for the operation of the system. The applied pressure is then controlled in an on or off state by a 12V pneumatic relay.

Due to current limitations in the control software and a recall of the rotary encoders used in the auger system, the motor is operated in an open loop setting. The user can adjust the speed of the motor with a manual speed regulator dial located on the robot while on/off/reverse status is controlled via a $\pm$ 10V signal from the Nservo to a relay switch. Future works will include monitoring and closed-loop feedback control for the feed-rate of the auger system.

Chapter 5

System Modeling and Control Design

This chapter will address the challenges associated with developing and implementing high precision motion control with a low-level control strategy via user-restricted control architectures. Precision motion control is often comprised of system identification and validation, along with subsequent controller design. As a legacy instrument which has gone through many – albeit dynamically insignificant – changes, the relevant system models and parameter verifications have been fleshed out in previous works but require updating and re-identification. The contents of Chapter 5 are organized in the following way: First, the linear model for each axis is provided from the modeled system dynamics. These dynamic models are then used in a closed-loop system identification technique to produce parameter estimates for each axis. The control design method for each axis of the XYZ positioning system is then outlined following discussion on the available architecture. Furthermore, system performance under these control strategies is compared against those of the derived linear models. A discussion on the performance of these controllers in the fabrication process of ferrite-epoxy cores is established in Chapter 6.

5.1 Plant Dynamics System Modeling

Each of the μRD axes is assumed to be dynamically decoupled from one another and modeled as sliding-mass systems which are described by the second-order differential equation shown in (5.1).

$$m\ddot{x} + b\dot{x} = F_{Total} \tag{5.1}$$

Here, x and it's derivatives represent an axis' position, velocity, and acceleration respectively; m is the inertial mass of the given axis; b is the associated viscous damping, F_{Total} is the resultant force produced from summing the thrust force generated at the motor, F_u, and the lumped disturbance forces, F_D:

$$F_{Total} = F_u + F_D \tag{5.2}$$

The resultant force of an axis in terms of the control input is given by (5.3) where K_{sys} is the gain of the mechanical system and u is the control input:

$$F_u = K_{sys} u \tag{5.3}$$

Plugging this into Eq(5.2) and substituting the result into Eq(5.1) gives the following dynamic equation form:

$$m\ddot{x} + b\dot{x} = K_{sys} u + F_D \tag{5.4}$$

5.1.1 System Disturbances

A combination of various electrical and mechanical phenomena contribute to the total disturbance force, F_D, that the μRD can experience. In all mechanical systems, the combination of these forces enter in nonlinear fashions, reducing the accuracy of linear modeling efforts and overall system performances. The main contributions of these disturbances for the μRD have previously been identified as frictional, cogging, and force ripple effects. The cogging effects were only present in the Z-axis due to the no-cog design of the X and Y linear stages. Previous plant model parameters are used to design feedforward control gains to initially compensate for some of these effects during the system identification process.

The electro-mechanical disturbance effects present in the μRD have been well documented by past research efforts [73], [76]. This section serves as a brief overview of these identified effects and causes. This work presents no new identification nor validations of these varied effects, but rather, attempts to compensate for them in a unifying model-based approach

– discussed later in this next section. These nonlinearities are modeled with a static mapping called the Force Ripple Map:

$$F_D = u_D(x, \bar{\dot{x}}) = \frac{f_{fric}(x, \bar{\dot{x}}) + f_{cog}(x)}{K_{sys}(1 - f_{FR}(x))} \tag{5.5}$$

Where $\bar{\dot{x}}$ denotes the system at a constant velocity; f_{fric} represents the combined nonlinearities of sliding friction; f_{cog} is the motor cogging effects; and f_{FR} is the contribution of the Force Ripples on the system.

5.1.1.1 Motor Cogging

Motor cogging occurs when the permanent magnet rotors of a motor experience a magnetic force attracting them to their magnetically permeable stators in an unpowered state [81], [82]. Since the X and Y-Axes have stators made from epoxy, which is not magnetically permeable, they experience no cogging effects. This is not the case for the iron-cored rotary motor of the Z-Axis.

5. 1.1.2 Frictional Forces

Frictional forces are well known disturbances within mechanical systems. This work and past works were specifically interested in the coulomb, viscous and Stribeck friction forces which make up the sliding friction within sliding mass systems such as the μRD. Figure 5.1 depicts the typical relation that these forces have to the dynamics of a system. In this standard model, the y-intercepts are the breaking point for the static friction between surfaces. As velocity increases (decreases), the system passes into the nonlinear region of Stribeck friction, followed by transition into a linear region during for the duration of the model. By fitting this linear region to an equation of the form $y = f_v * \dot{x} + f_c$, the viscous and coulomb friction can be taken as the slope f_v and y-intercept f_c. Figure 5.2 shows an example of this sliding friction identified in [Bristow].

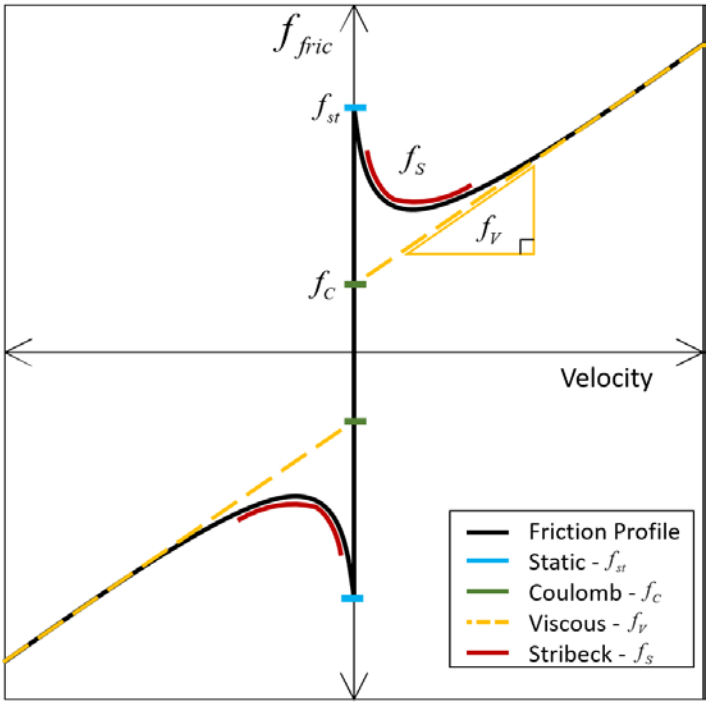

Figure 5.1 Stribeck-type sliding friction model.

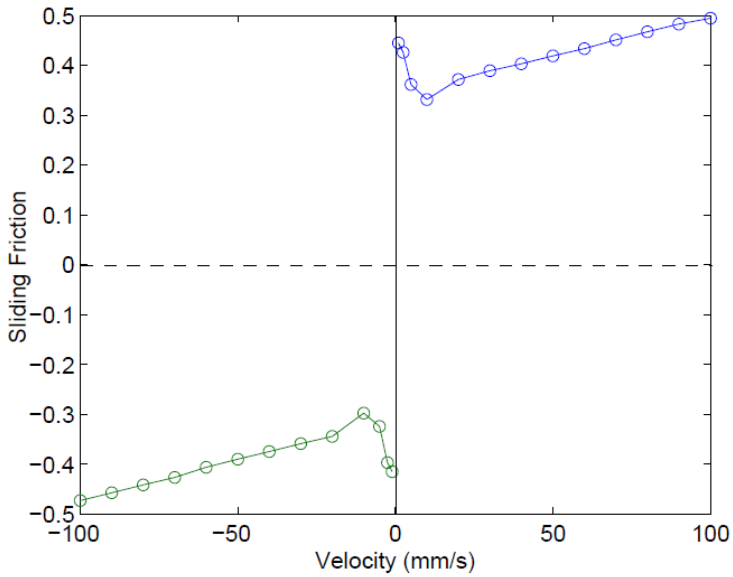

Figure 5.2 Estimates of the sliding friction forces present in the X-Axis matching a Stribeck sliding friction model [73]

5.1.1.3 Force Ripples

Force ripples arise in linear motors due to imperfections of the electromagnetic components responsible for actuating the system. The reality of the Hall Effects from the servo-amplifiers along with the nonuniformity of the fields created by the permanent magnets within the linear motor result in these nonlinear behaviors. These force ripples can be represented as the sum of several sinusoidal operations with varied amplitudes and frequencies that strictly depend on the position of the linear stage. One can see the effects of these force ripple in a Force Ripple Map such as Figure 5.3. The force ripple map is named as such because the most identifiable component of the map is in-fact the force ripples.

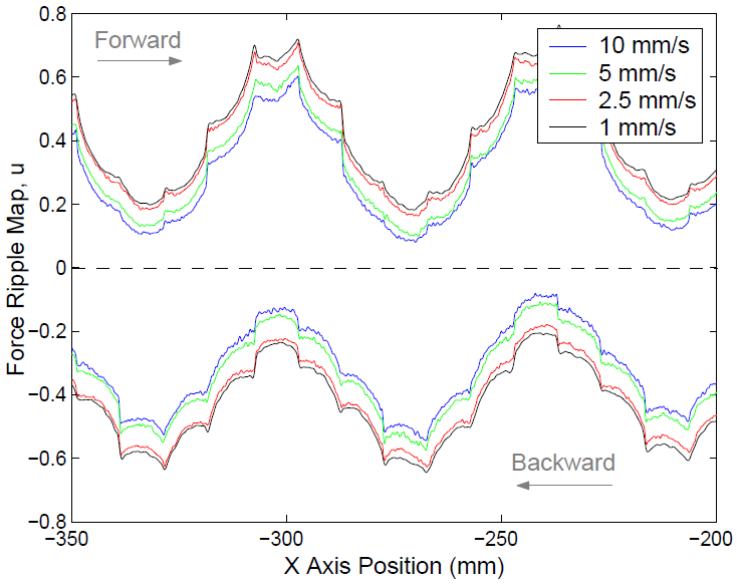

Figure 5.3 Force Ripple Map for the X-Axis at varied speeds; reprinted from [73]

Due to limitation of the A3200 software, compensating for these nonlinearities is not easily handled. Accommodations are only made for a single value of static friction compensation, which is applied equally either direction of motion. This does not allow for standard sliding friction compensation nor the advanced Force Ripple Mapping techniques to be implemented during system identification. To overcome this, a predictive strategy called feedforward is used. This work, however, neglects these disturbances at the time of system identification and shows that well-performing, low-level compensators may be designed by looking at normalized outputs in the system identification process. Due to the orders of

magnitude differences in system model gains, these feedforward techniques are implemented at the end of the controller design process once the appropriate updated models have been identified.

5.1.2 Plant Models

All electro-mechanical positioning system can be more accurately described using nonlinear models and increasing orders of dynamics. This work assumes that the linear models presented are sufficiently accurate for the purposes of both system identification and feedback control design discussed in section 5.2.1. This assumption is made based on the fact that operating speeds are not fast enough to excite high frequency resonances. Neglecting the nonlinearities at this stage is synonymous with setting $F_D = 0$ in Eq (5.4) leaving a strictly linear model of the plant dynamics:

$$m\ddot{x} + b\dot{x} = K_{sys}u \tag{5.6}$$

Taking the Laplace transform of Eq (5.5) for each axis produces a frequency domain plant model of the form:

$$G_p(s) = \frac{X(s)}{U(s)} = \frac{K_m}{s*(\tau_m s+1)} \tag{5.7}$$

The model defined by G_p gives the input-output the relation between the position of a given axis and the command signal from the controller. Here, K_m is assumed to represent all gains of the system including those from the servo amplifiers, any digital-to-analog converters along the signal path, and the damping that is not included previously with K_{sys}. Representing the systems in this manner leaves two parameters to be identified: the mechanical time constant, τ_m, and the steady-state gain of the system, K_m. By first differentiating Eq (5.6), a first-order model representation for the velocity of a given axis is:

$$G_v(s) = \frac{K_m}{\tau_m s+1} \tag{5.8}$$

5.2 System Identification

Operating conditions required by the A3200 software turned out to be the limiting factor when choosing the system identification technique implemented in work. First, the closed loop architecture of the software precludes any open-loop system identification techniques. Operating in this closed-loop environment requires the feedback loop gains $\{K_p, K_i, K_{p1}, K_{pi}, K_{d1}, K_{pos}\}$ to be set during system identification. For simplicity of calculation and ease of methodology K_{p1} was the only parameter used during the system identification phase – with all other parameters set to 0. These parameters are defined explicitly in section 5.3 with the discussion on controls.

5.2.1 Logarithmic Decrement Technique for Parameter Estimation

The logarithmic decrement technique is a well-established technique used for closed-loop system identification by examining a second order system's time-domain response to a step-input [83]–[86]. Although this technique does not directly offer the parameters K_m and τ_m that are required to describe the systems, they can be determined from their mathematical relationship with second order response characteristics such as the damping ratio and natural frequency that this technique identifies.

Implementing the logarithmic decrement technique requires a system to produce a decaying oscillatory transient response to the step-input. The position-loop proportional gain K_{p1} is increased until an adequate response is achieved. To produce a position step response in the A3200 environment, the RAPID motion command is utilized. In practice, the command is given as RAPID [Axis] [Distance] (e.g. RAPID X 1). From this oscillatory response, the logarithmic decrement parameter, δ, can be computed from the following equation:

$$\delta = \frac{1}{k}\sum_{i=1}^{k}\frac{1}{n_i}\ln\left(\frac{x(t)}{x(t+n_iT)}\right) \tag{5.9}$$

As shown in Figure (5.4), $x(t)$ is the response amplitude at time t in seconds; $x(t+n_iT)$ is the amplitude at the n_i-th peak away; T is the average time in seconds between

any two adjacent peaks; k the number of successive peak responses used in the calculation, with integers $n_i, k \geq 1$.

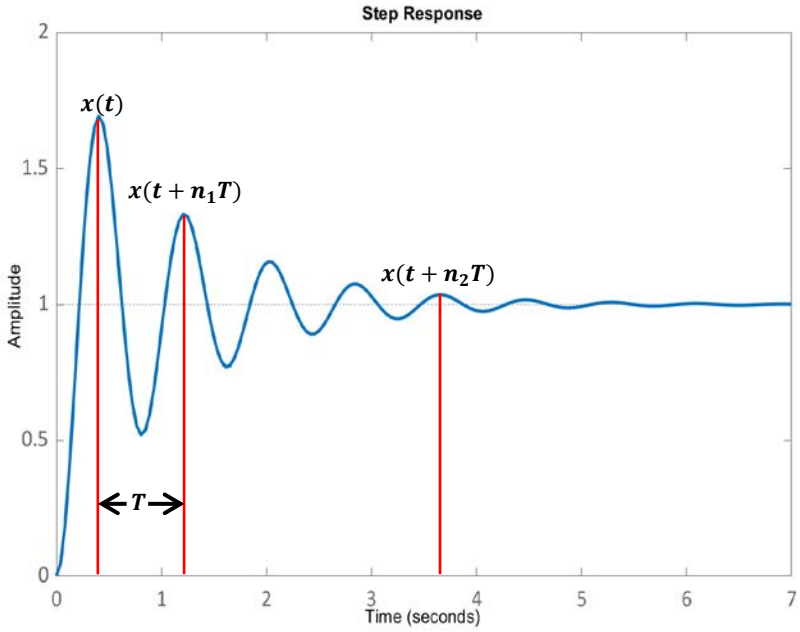

Figure 5.4 Logarithmic decrement technique step response with $n_1 = 1, n_2 = 4, k = 2$.

The damping ratio, ζ, and natural frequency, ω_n, are then calculated from the logarithmic decrement found in Eq (5.9) using the following relations:

$$\zeta = \left(1 + \left(\frac{2\pi}{\delta}\right)^2\right)^{-1/2} \tag{5.10}$$

$$\omega_n = \frac{2\pi}{T\sqrt{1-\zeta^2}} \tag{5.31}$$

Let $\overline{K}_{p1}$ represent the proportional gain used to create the oscillatory responses during system identification. The time constants and motor gains are computed by equations (5.12) and (5.13). This technique was applied to each axis five times with the resulting values were averaged to generate the constants used for the system models in this work. These values are provided in Tables (5.1) – (5.3).

$$\tau_m = \frac{1}{2\zeta\omega_n}, \qquad K_m = \frac{{\omega_n}^2 \tau_m}{\overline{K}_{p1}} \tag{5.12, 5.13}$$

Table 5.1 X-Axis system parameters from logarithmic decrement implementation.

System Model	Trial	τ_m	K_m
$\frac{K_m}{s(\tau_m s+1)}$	1	0.5498	2731400
	2	0.5835	3022580
	3	0.5874	3171570
	4	0.6004	3108000
	5	0.4449	2041130
	Mean	0.5533	2814930

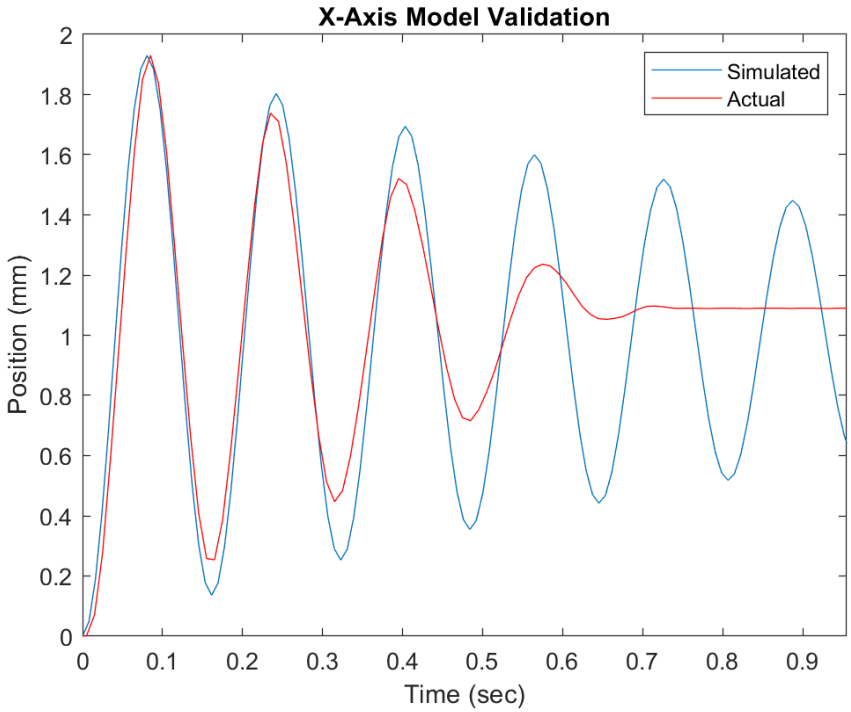

Figure 5.5 Oscillatory step response and matching simulated response for the X-Axis using model parameter estimates from Table (5.1).

Table 5.2 Y-Axis system parameters from logarithmic decrement implementation.

System Model	Trial	τ_m	K_m
$\frac{K_m}{s(\tau_m s+1)}$	1	0.3412	4173740
	2	0.2366	2161630
	3	0.2080	1597850
	4	0.2351	2248520
	5	0.4555	3974530
	Mean	0.2953	2831250

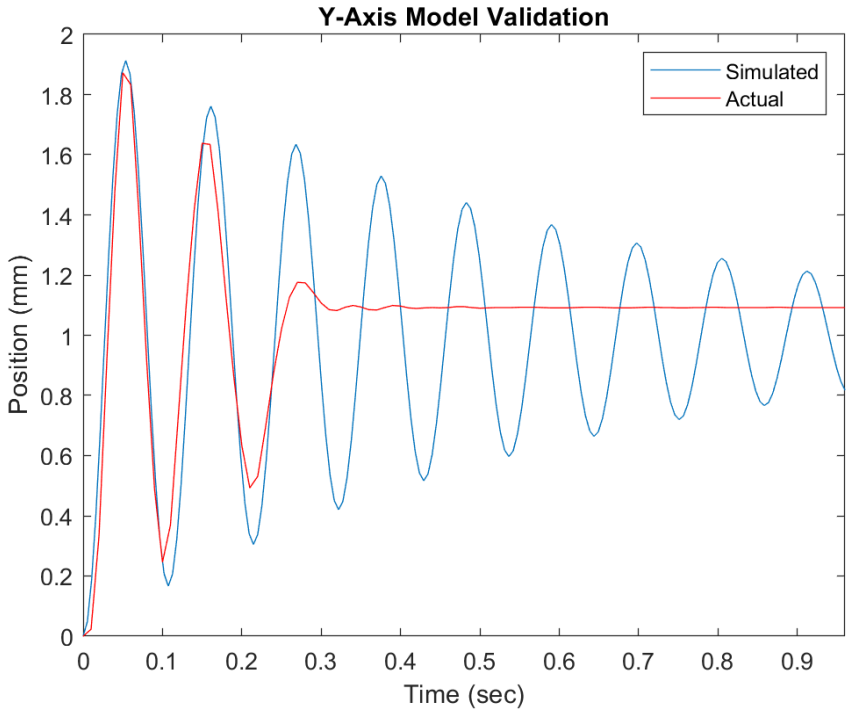

Figure 5.6 Oscillatory step response and matching simulated response for the Y-Axis using model parameter estimates from Table (5.1).

Table 5.3 Z-Axis system parameters from logarithmic decrement implementation.

System Model	Trial	τ_m	K_m
$\frac{K_m}{s(\tau_m s+1)}$	1	0.0950	13984600
	2	0.0763	16179600
	3	0.0898	15741600
	4	0.0809	14187600
	5	0.0811	11942200
	Mean	0.0846	14407100

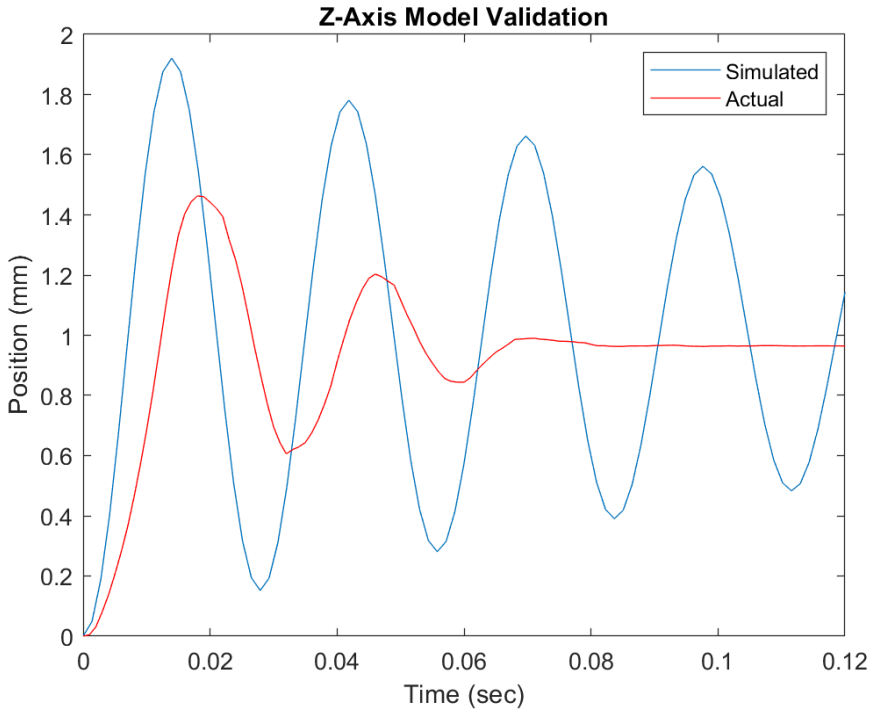

Figure 5.7 Oscillatory step response and matching simulated response for the Z-Axis using model parameter estimates from Table (5.1).

The reader should note that once the system is producing less energy than is required to overcome the static friction, it will “grab” the stage at that position. This can be observed

when the oscillatory response becomes small and a constant steady-state error is produced. For this reason, attempt to produce enough oscillations while using the first few cycles for analysis before the energy in the system dissipates.

5.2.2 Model Verification and Tuning

The models built using the identified parameters are shown against samples from the system identification method in figures (-). The models are seen to be significantly underdamped in comparison to the experimental responses. The Z-axis is also observed to have a small – albeit significant – time delay. Logarithmic decrement assumes the system being inspected is purely linear. However, all mechanical systems have some degree of nonlinearity. To account for these nonlinearities of these dampened responses, a damping term β is introduced to the models as in Eq (5.14); the model for the Z-axis is further modified to include the time delay term Eq (5.15). The time delay constant τ_d is in the units of seconds. These modified parameters are fit by hand to match the normalized step responses from figures (5.7-5.9)

$$G_{P_k} = \frac{K_m}{s(\tau_m s + \beta)} \qquad k \in \{X, Y\} \tag{5.14}$$

$$G_{P_Z} = \frac{K_m e^{-\tau_d s}}{s(\tau_m s + \beta)} \tag{5.15}$$

Table 5.4 Damping and time delay parameters used to match normalized experimental and simulated responses.

Axis	β	τ_d
X	2.15	0
Y	2.25	0
Z	17	0.0025

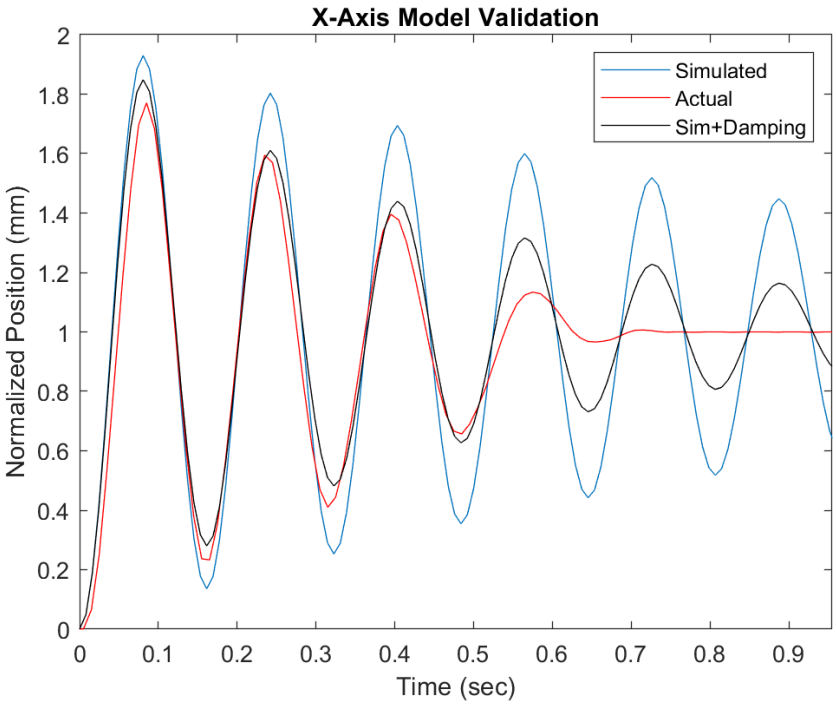

Figure 5.8 Normalized X-axis model validation.

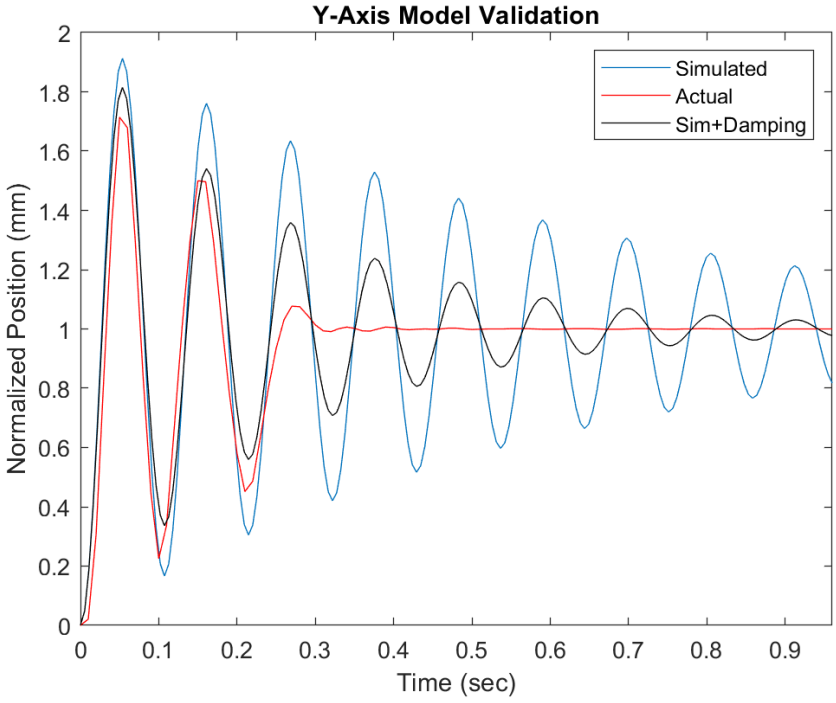

Figure 5.9 Normalized Y-axis model validation.

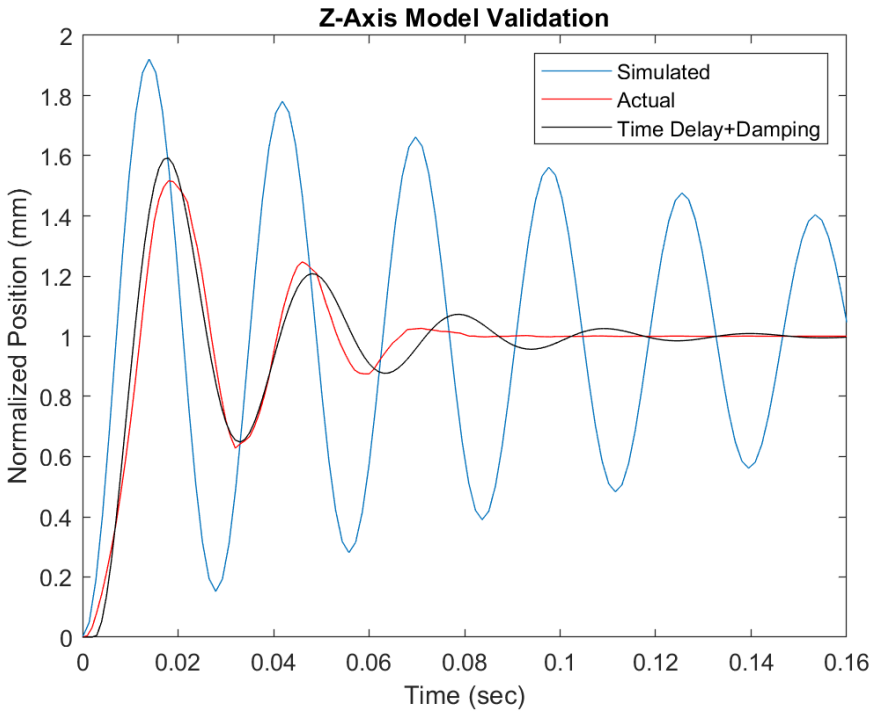

Figure 5.10 Normalized Z-axis model validation.

5.3 Control Architecture

Operating within a high-precision domain of additive manufacturing requires a well-tuned control strategy to be designed and implemented on the μRD system. As previously mentioned, the A3200 environment is responsible for providing the main control architecture. The architecture presented in this work consists of three main elements: 1) a position feedback controller; 2) a velocity feedback controller; and 3) a set of static feedforward gain compensators. These three elements are summed together to provide the control input (Amps) to system or plant for a given axis. The position and velocity feedback controllers are coupled in a dual-loop fashion; meaning the controller has the ability to compensate both while neither rely on the output signal of the other, as opposed to the cascaded control approach found in similar systems. Figure (5.10) shows a summary of this architecture with some associated signals.

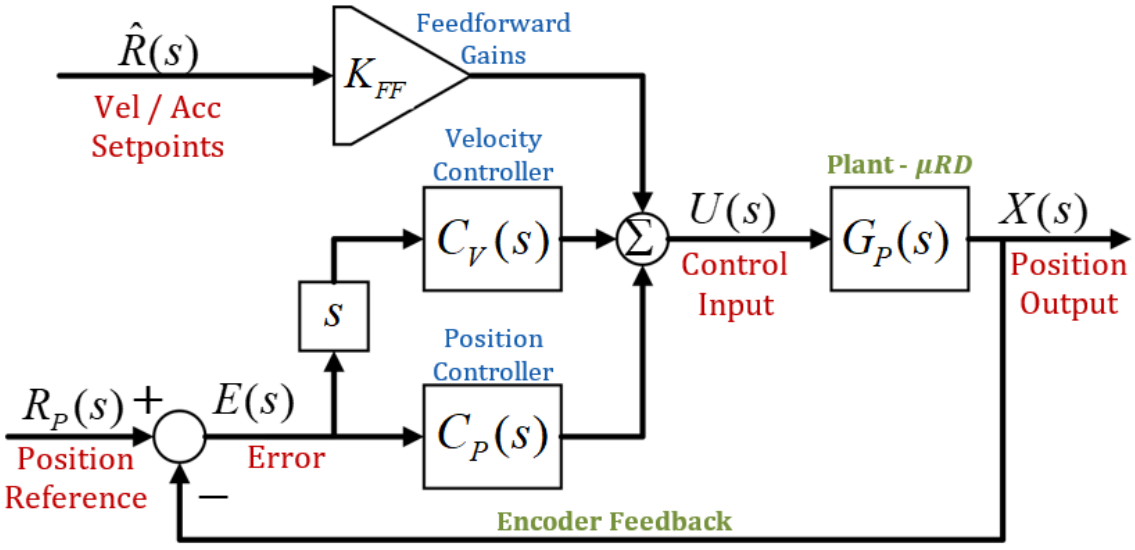

Figure 5.11 Representative block diagram for the A3200 control architecture. Red signifies various signals sent or received in the system; Blue labels represent control elements available for design; Green indicates moving elements or sensors within the system.

This work focuses on the design of a velocity controller, $C_V(s)$, as the main strategy of feedback compensation for each axis of the μRD system. This author's decision to focus on the control of velocity in this work stems from the nature of the motions and end results desired during operation. In other precision motion applications, users may only be interested in the end position or certain intermittent positions of the task being precisely achieved at a desired time. In extrusion-based AM however, the user is concerned with maintaining the correct velocity over the entirety of the task. Should the system speed up or slow down too much while attempting to maintain its position, the material paths risk thinning or clumping either of which are undesirable to the fabrication process.

The following sections will present a model reduction of the architecture provided allowing for design of this velocity compensator:

- A velocity PI controller designed via root locus techniques
- Nominal inclusion of the position loop for improved position tracking
- A method for designing the feedforward gains via an inverse-plant model.

5.3.1 Model Reduction for Velocity Control

For design of the velocity controller, a reduced model from that given in figure (5.10) is needed. First, the feedforward compensator is simply a set of static gains which can all be set to zero. Further, by substituting the velocity plant, $G_V(s)$, in to Eq (5.7) for the position plant model, we can replace the plant model by two separate blocks – the velocity plant and an integrator:

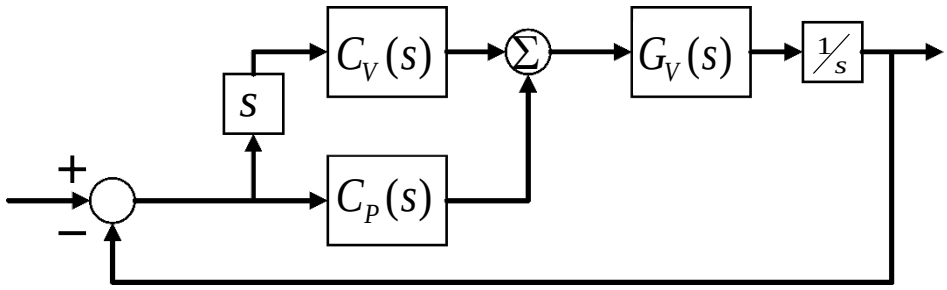

Figure 5.12 Representative block diagram isolating the dual loop feedback of the A3200 control architecture

The position controller $C_P(s)$ is a PID controller. Thus, the model can be further reduced by setting each of the P, I and D gains of this to zero, in effect contributing 0 at all times and eliminating the need for summing control signals. This is done in the A3200 environment by setting the parameters $K_{p1} = K_{pi} = K_{d1} = K_{pos} = 0$, where the first three are the usual PID terms and K_{pos} is a term used for resolution discrepancies within the A3200 software. By canceling the frequency domain derivative and integrator terms the following reduced model is yielded in terms of just the velocity controller and velocity plant:

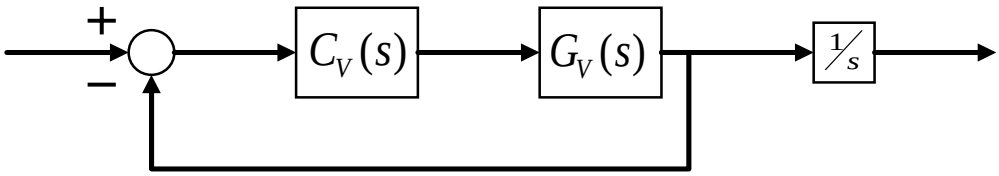

Figure 5.13 Block diagram reduced to the velocity controller and first order velocity plant used in PI controller design.

One can notice that this representation allows for the reference signal to now be given as a velocity command R_V. Typical closed-loop control design techniques can be used to shape the velocity performance of the μRD axes using this block structure in MATLAB and Simulink. The position profiles may also be easily extracted from this architecture as seen by the integration of the velocity output signal outside of the feedback loop.

5.3.2 Velocity Feedback Control Design

The A3200 environment is what dictates the control strategy for the velocity loop given by figure (5.12). In this, the velocity feedback controller $C_V(s)$ takes the form of a PI controller. As depicted in the block diagram – and is the case in usual PID structures – the PI controller operates on the error signal generated from the difference in the reference signal given to the system and the actual output that is detected by the sensors. The sensors on the μRD happen to be real-time optical encoders which can determine the position of the axis (in encoder counts) and the A3200 environment is able to translate this in to the corresponding velocity.

The acronym PID stands for Proportional-Integral-Derivative, each term of which is derived from the way the controller's three terms act on this error signal. The same logic holds for the PI control strategy that C_V follows. The proportional term adds an amount of control signal to the input that is directly in proportion to the error, call it K_P. The integration term continuously integrates the error signal and adds a control input that is proportional to this amount, call it K_I. Combining these ideas gives the controller its transfer function form:

$$\begin{aligned} U(s) &= K_P * E(s) + K_I * \left(\frac{1}{s} E(s) \right) \\ &= \left(K_P + K_I * \frac{1}{s} \right) * E(s) \\ &= C_V * E(s) \\ \\ \Rightarrow C_V &= K_P + \frac{K_I}{s} \end{aligned} \tag{5.16}$$

Root locus design techniques were used to design the controllers for each axis. The technique uses the open-loop poles and zeros to inform closed loop stability and performance. To properly use this technique, C_V is first put into a zero-pole form:

$$C_V = K_P\left(\frac{s+T_I}{s}\right) \tag{5.17}$$

Where the integral ratio $T_I = K_I/K_P$ represents the zero placement of the controller and K_P is the only gain left to be varied over the root locus design. Using the Control System Designer toolbox in MATLAB, the controller zeros and gains for each axis were chosen so that the following design criteria were met: 1) Stability – closed loop poles must all lie in the left-half of the complex plane, $\mathbb{C}$; 2) 5% settling time within 0.1 second and 2% settling time within 0.25 seconds; 3) maximum overshoot of 25%. The resulting control parameters are given in Table (5.5) along with the simulated step responses; the green bands shown indicate the 2% settling region.

Table 5.5 PI controllers designed in simulation using the system models for each axis.

Axis	K_P	K_I
X	$2.37*10^6$	34069
Y	$1.67*10^6$	17744
Z	56000	1925

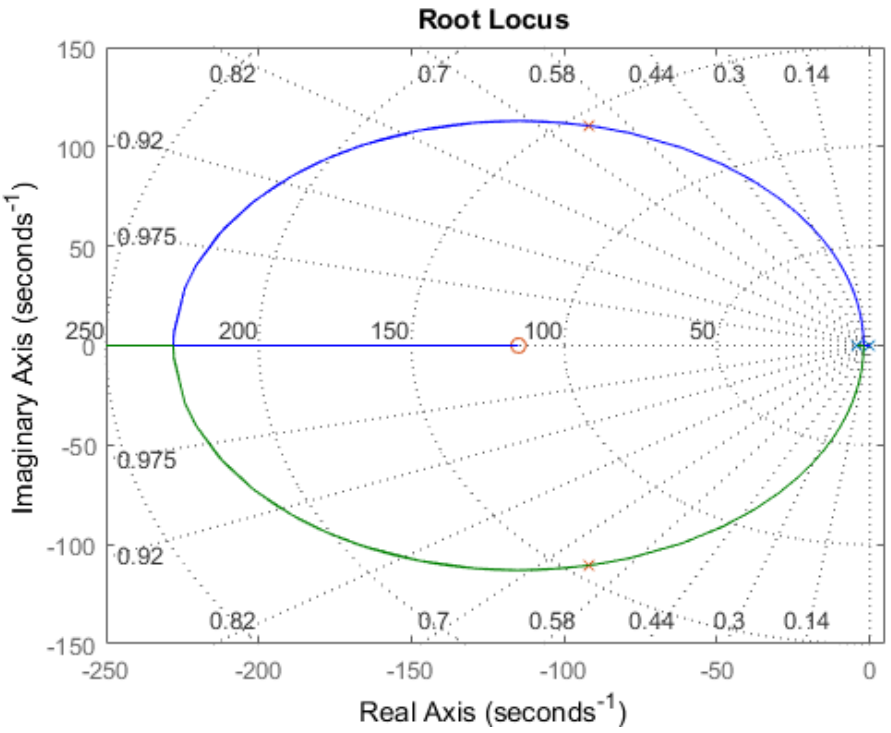

Figure 5.14 X-Axis PI controller root locus design. Blue 'X's and 'O's indicate open-loop poles and zeros; Red 'X's and 'O's indicate closed-loop poles and zeros.

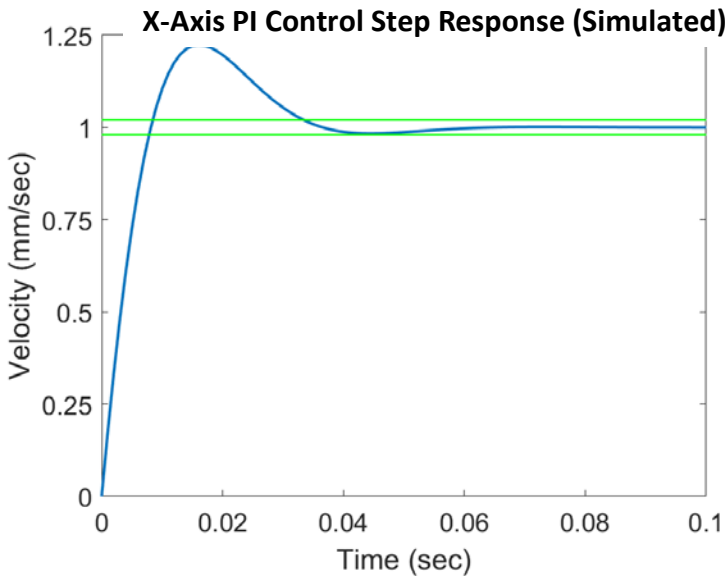

Figure 5.15 X-Axis PI controller simulated step response for 1 mm/s command.

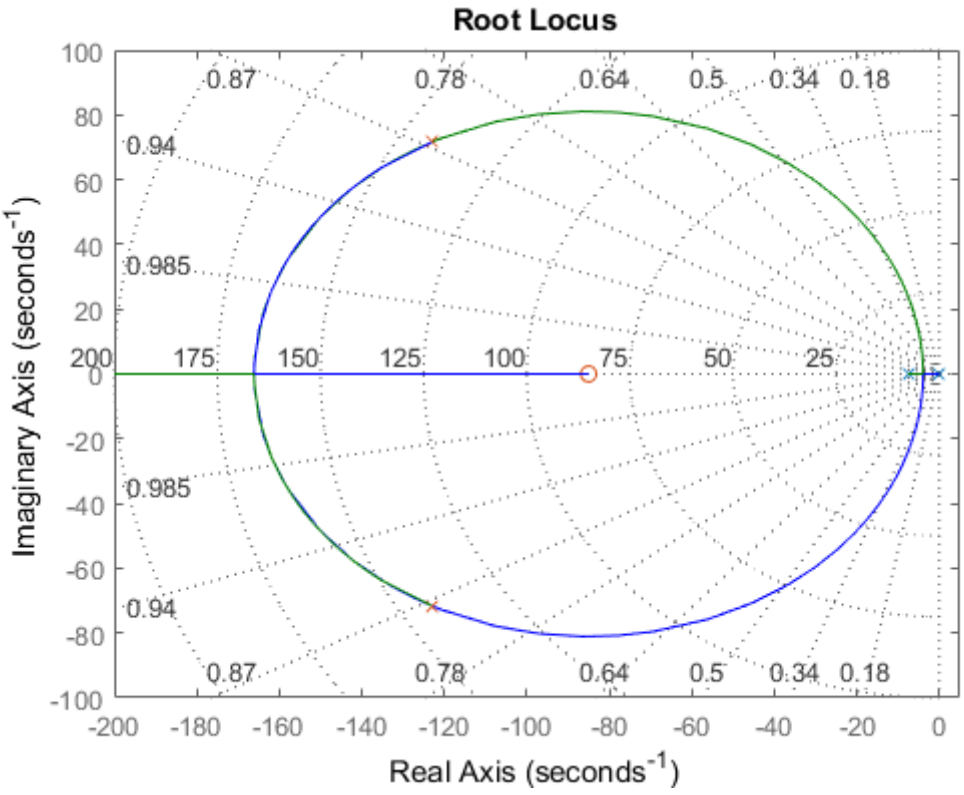

Figure 5.16 Y-Axis PI controller root locus design. Blue 'X's and 'O's indicate open-loop poles and zeros; Red 'X's and 'O's indicate closed-loop poles and zeros.

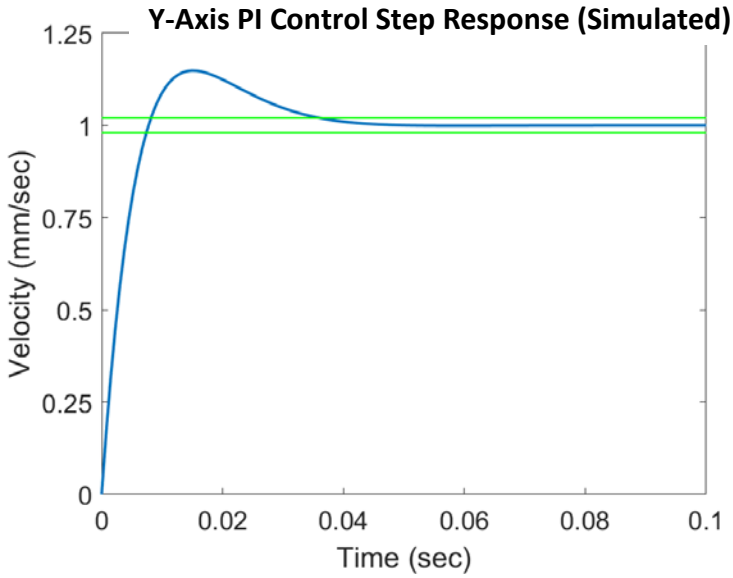

Figure 5.17 Y-Axis PI controller simulated step response for 1 mm/s command.

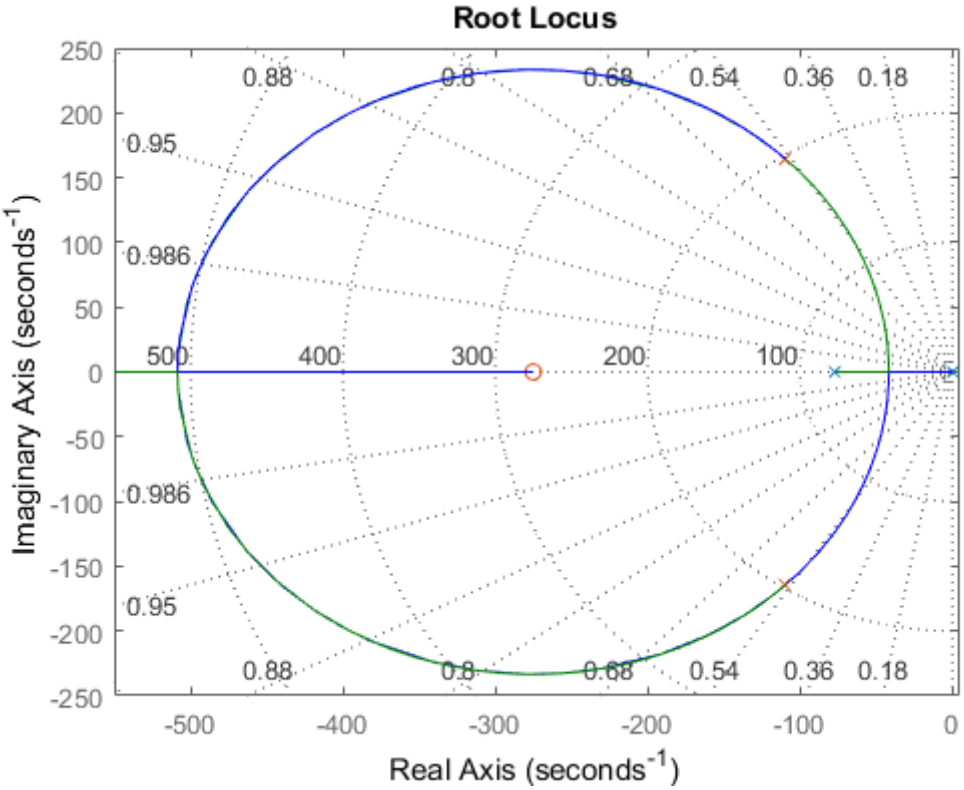

Figure 5.18 Z-Axis PI controller root locus design. Blue 'X's and 'O's indicate open-loop poles and zeros; Red 'X's and 'O's indicate closed-loop poles and zeros.

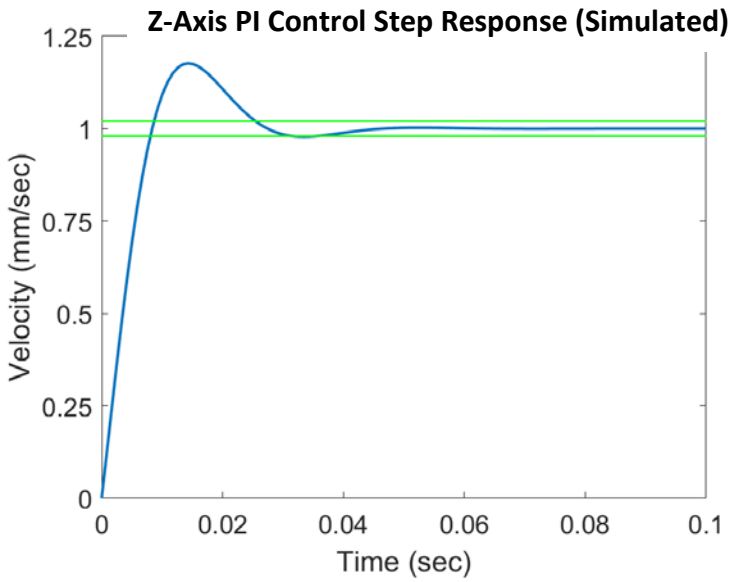

Figure 5.19 Z-Axis PI controller simulated step response for 1 mm/s command.

Before implementing these controllers on the μRD, each of the controllers are modified to include a nominal position error integrator term. To do this we can first refer to the block diagram of the system in figure (5.12) and reintroduce the position controller. Keeping the velocity focus of the block diagram means introducing an additional integrator to the loop before the position controller in order to transform the passing signals back to position reference units, see figure (5.16). By only including the integral term of the position controller we have a new controller given by Eq (5.18), where the velocity integrator ratio $T_I = z_1 + z_2$ and the new position integrator ratio $T_{pi} = K_{pi} / K_P = z_1 * z_2$, are given in terms of the zero placements.

$$\bar{C}_V = K_P + \frac{K_I}{s} + \frac{K_{pi}}{s^2} = K_P \frac{(s+z_1)(s+z_2)}{s^2} \tag{5.18}$$

The same design process was used to develop this new controller; the zero placement of z_1 and proportional gains from the previous controllers remain the same while z_2 is placed between the open-loop system pole and the origin to ensure a comparatively small contribution from this position integrator term. The parameters used for this new controller scheme are shown in Table (5.6).

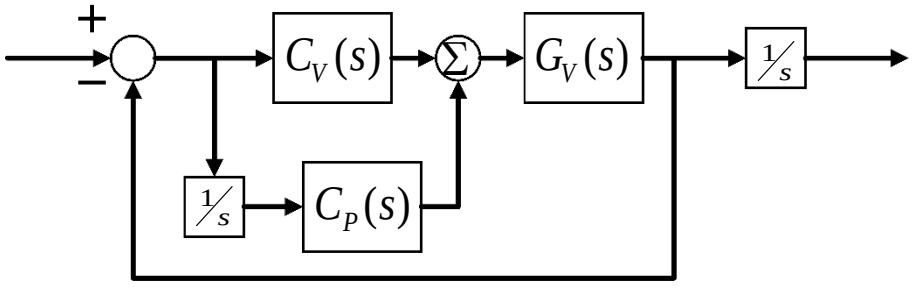

Figure 5.20 Block diagram of the combined velocity feedback controller with nominal position integrator compensator for the first order velocity plant.

Table 5.6 Position integrator augmented velocity controllers for each axis.

Control Scheme	Axis	K_P	K_I	K_{pi}
$\bar{C}_V = K_P + \frac{K_I}{s} + \frac{K_{pi}}{s^2}$	X	$2.37*10^6$	35254	130
	Y	$1.67*10^6$	18370	51
	Z	56000	1943	46

These controllers were implemented on the μRD for each of the corresponding axes and velocity step responses were taken. Each axis received a reference signal of 10 mm/s over a distance of 5 mm in the X and Y-directions and 10 mm in the Z-direction before removing the signal. The results are shown in the following figures (5.17-5.19).

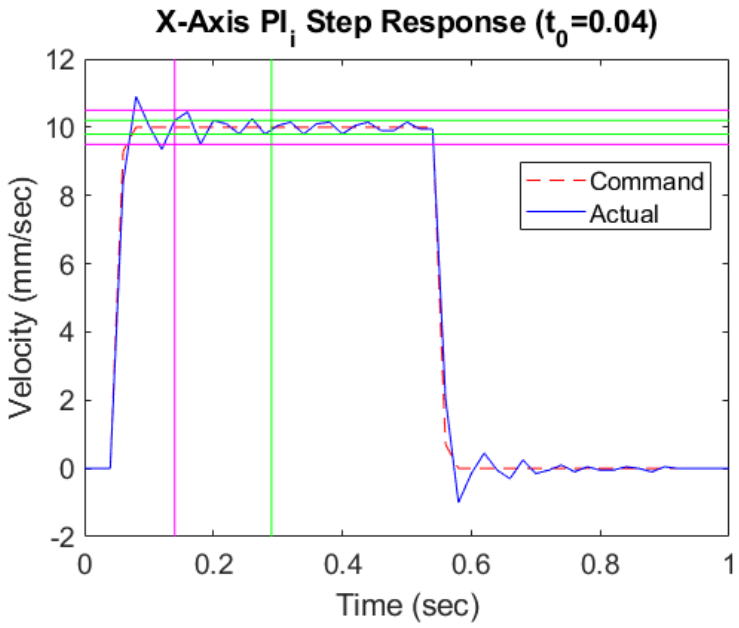

Figure 5.21 Step response performance to a 10 mm/s command for the X-Axis with the control scheme and gains identified in Table (5.6).

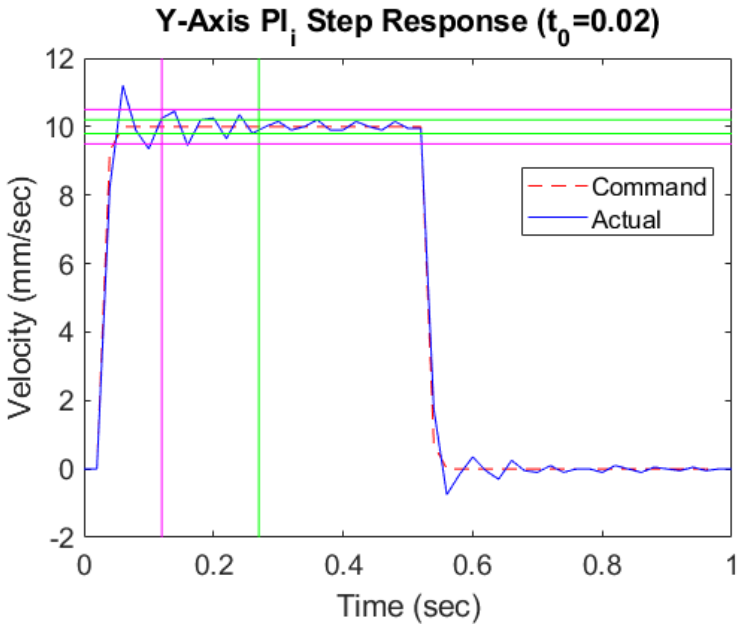

Figure 5.22 Step response performance to a 10 mm/s command for the Y-Axis with the control scheme and gains identified in Table (5.6).

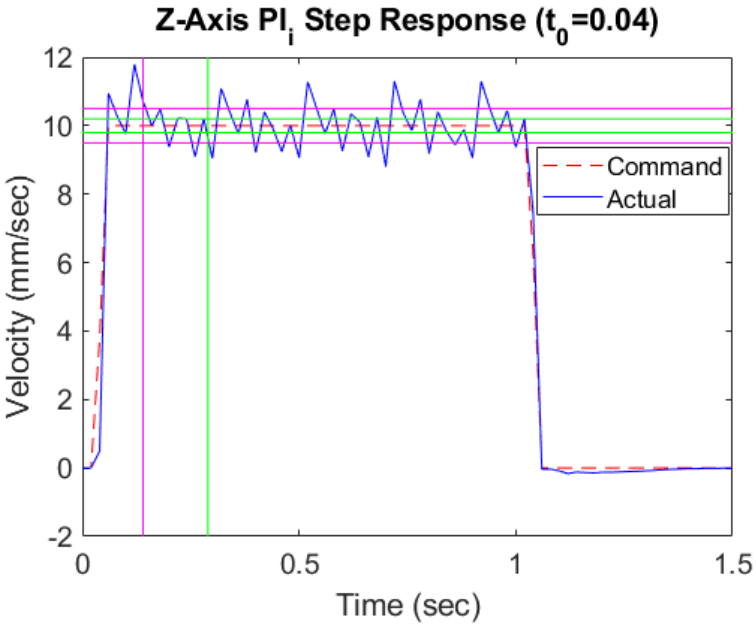

Figure 5.23 Step response performance to a 10 mm/s command for the Z-Axis with the control scheme and gains identified in Table (5.6).

There are small delays between when the system began recording data and the commands are sent/received. These delays are noted and the initial command time t_0 is given in the figures. The vertical and horizontal magenta lines represent the desired 5% settling time (0.1 sec) and region, respectively; green indicates the same metrics for 2% settling. One can see from the figures that the X and Y-axes both meet our requirements. The Z-axis, on-the-other-hand, has considerable periodic oscillation in the steady state. This author argues that this will not affect overall fabrication performance since the nature of this method of AM relies on dynamic motion in the XY plane while the Z-axis serves to provide stable heights during the XY-motion. For this reason, the performance of a position step response for this controller is examined by replacing the 5% settling requirement with a stricter 0.5% steady-state error bounding (2% settling requirement remains). This is displayed in Fig (5.20).

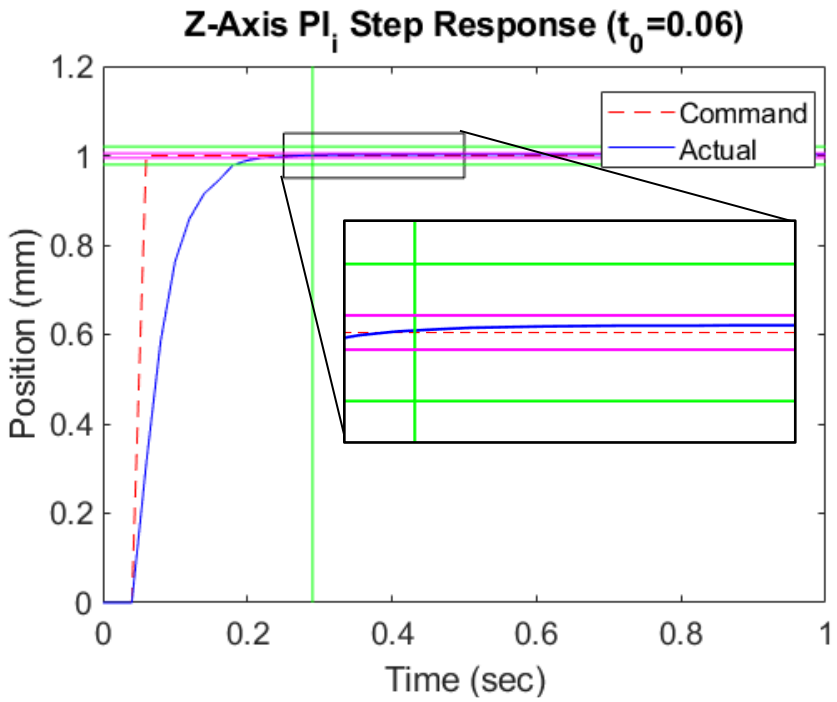

Figure 5.24 Step response performance to a 1 mm position change command for the Z-Axis with the control scheme and gains identified in Table (5.6).

Chapter 6

Fabrication Results and Conclusions

This chapter presents the performance of the controllers designed in chapter 5 through the fabrication of ferrite toroidal cores. The resulting components are then analyzed along with the feedback data of the controllers to determine successful toolpaths and component fabrications. The performance of the μRD system is evaluated based on these results.

6.1 Target Fabrication Structure

As discussed in Chapter 2, the target structures for this work are rectangular toroids as in Figure 6.1(a). These structures will be constructed from alternating layers of clockwise and counter-clockwise, concentric circles. An example of the toolpath is given in Figure 6.1(b). The system is programmed to extrude material only during the circular motion sections of the toolpath (i.e. no material is deposited when transitioning between concentric circles nor between layers).

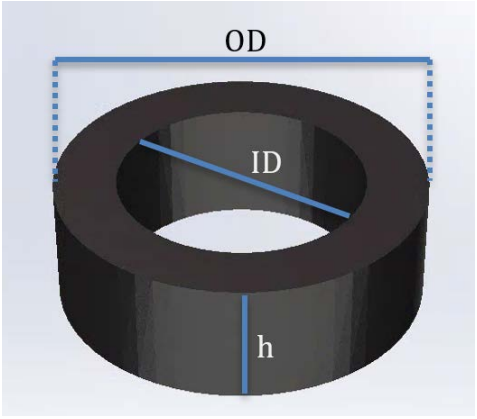

Figure 6.1 CAD rendering of an example structure to be constructed

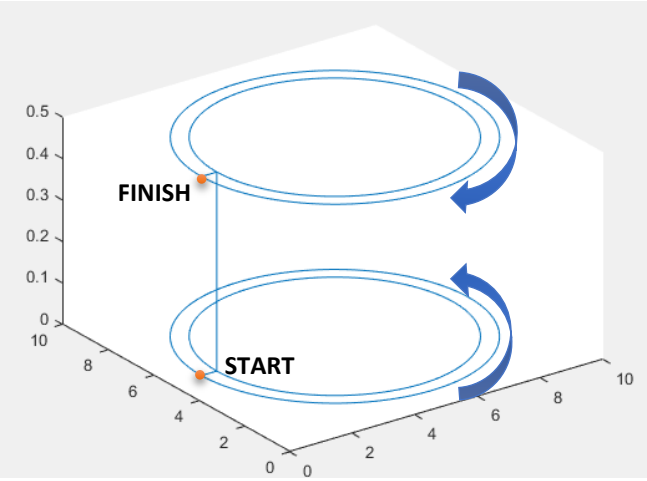

Figure 6.2 Sample μRD toolpath trajectory for a 2 layer, 2 circle-width toroid

A CAD rendering such as the one in Figure 6.1 is made using Solidworks and then converted to an STL file to be sliced. This work utilizes the slicing software CraftWare to generate the accompanying G-Code base imported to the A3200 environment that is used for manufacturing these structures. A screenshot of the G-Code being inspected within the CraftWare environment is shown in Figure 6.2.

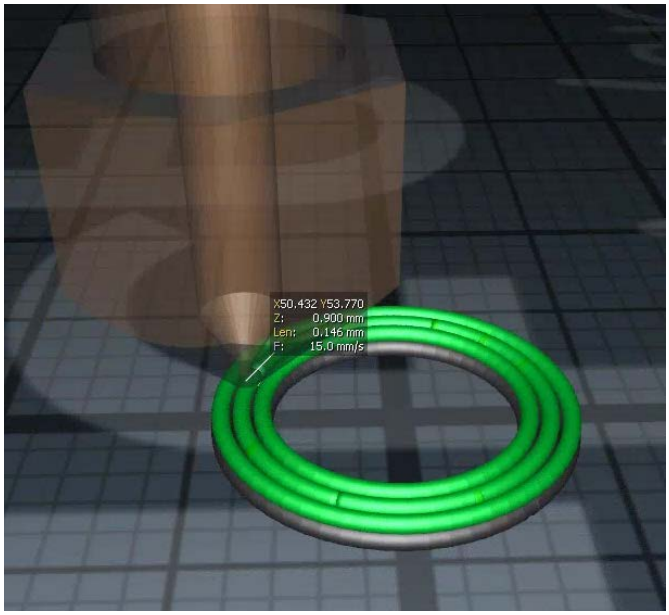

Figure 6.3 Screen grab of the G-Code generated toolpath using CraftWare.

6.2 Position Tracking Performance

This section focuses on evaluation of the tracking performance of the controllers designed for the X and Y-Axes. We accomplish this by introducing the biaxial contour error as our deterministic measurement. Biaxial contour error differs from a traditional reference tracking error by evaluating the minimum linear distance between the feedback position and the reference trajectory. If we were to measure instead the error between the reference position and the feedback position as in traditional reference tracking, we may introduce additional time lag or lead that a system may experience. This gives a better evaluation of where material is eventual extruded compared to the desired build location within the manufacturing process. Figure 6.3 displays these differences in tracking errors.

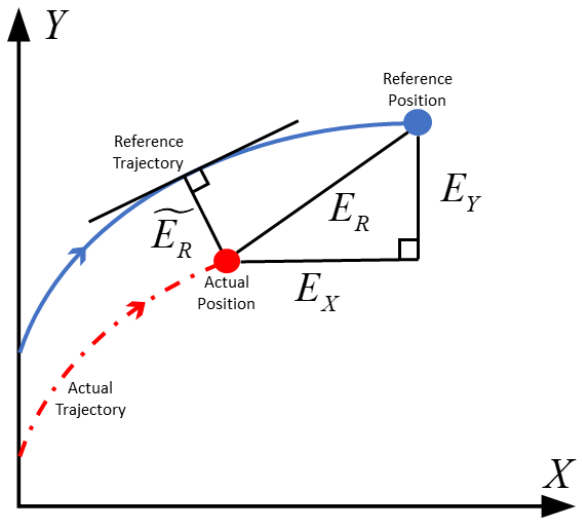

Figure 6.4 Biaxial contour error.

The blue line and dot indicate the reference trajectory given to the system and the current reference position at some time, respectively. The red line and dot indicate the reference trajectory given to the system and the current reference position at some time, respectively. E_R is the traditional tracking error described by the R^2 value taken from the Y-Axis position error E_Y and the X-Axis position error E_X. The Biaxial contour error is the shortest linear distance indicated by $\widetilde{E_R}$.

One can note that we do not include the Z-Axis with our contour error determination, as it is assumed that with material extrusion type AM the material will be deposited beneath the nozzle, laying upon the previous layer or substrate, despite any positional perturbations. Errors in the component contour that are not directly due to the positioning system would be associated with either ink synthesis, such as lack of appropriate ink rheology and/or incorrect zeroing of the stage.

6.2.1 Biaxial Contour Error Mapping

Since the toolpaths consists predominantly of circular motion, the X and Y-Axes will be tracking sinusoidal trajectory profiles in both velocity and position. From here on, print speed will refer to the combined angular velocity of the X and Y-Axes (i.e. the amplitude of the sinusoidal reference velocity). We investigate the same toolpath contours as are used in the fabrication of the final components. The structure to be fabricated is a 9 x 6 x 3 mm (OD/ID/height) toroid. The nozzle used has an inner diameter of 0.5 mm which produces a toolpath contour containing 6 layers of 3 concentric circles.

To analyze the contour tracking we generate a mapping scheme for the biaxial contour error. This mapping plots the three-dimensional reference toolpath and combines it with the magnitude of the biaxial contour error associated with each (x, y) pairing on the path. The biaxial contour errors are presented an overlaying heat map to the generated toolpath. The intensity of the heat map is a scaling from 0 to the maximum biaxial contour error over the toolpath in μm associated with the legend to the right of the plots.

We first generate the biaxial contour mapping for a low print speed of 1 mm/s, shown in Figure 6.4. For this print speed we have the contour error ranging from a minimum of 0.035 μm to a maximum at 41.7 μm with an average of 4.16 μm, when taken over the entire contour.

What is interesting to note is that the maximal error occurs periodically near the maximum amplitude of the y-direction motion, $\frac{(2n-1)\pi}{2}$ for each concentric circle where $n \in \{1, 2\}$. Inspection of the Y-Axis position and velocity profiles provide strong evidence that this is the result of stiction when attempting to initiate motion out of a zero-velocity state

regardless of the sign of direction (see Figure 6.5). This may be due to the nonlinearities that are neglected in the system identification steps. The offset angle seen between layers is from the alternating direction of concentric circles.

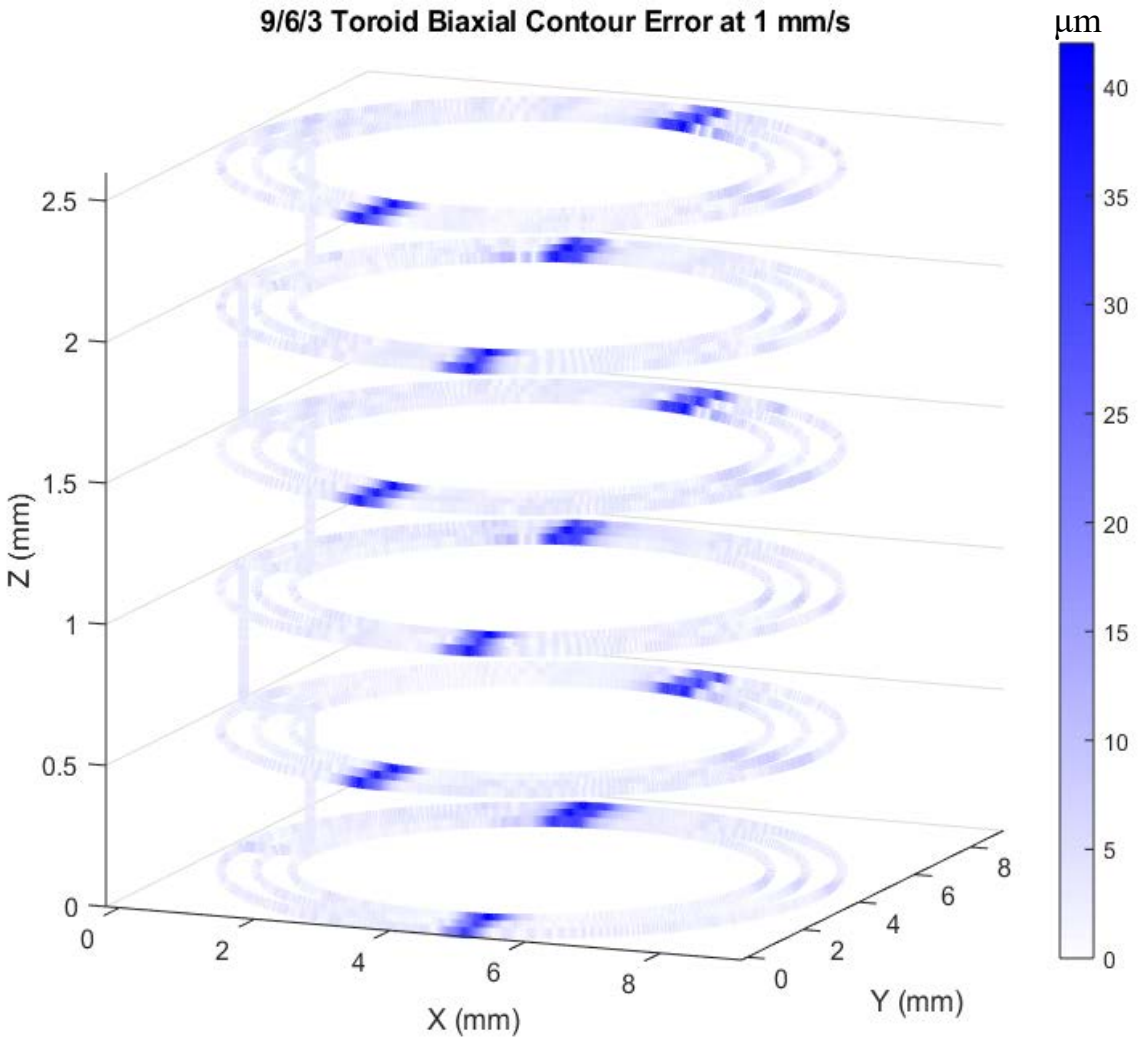

Figure 6.5 Biaxial contour error map for print speed of 1 mm/s

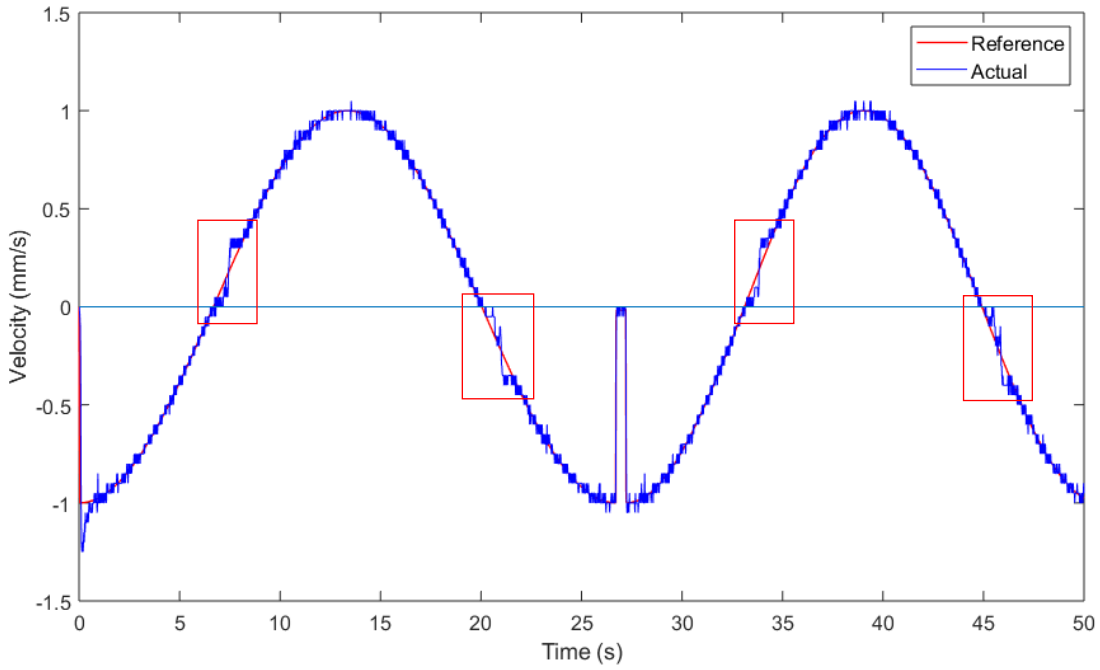

Figure 6.6 Y-Axes velocity tracking profile at 1 mm/s for a single layer of concentric circles, red boxes indicating regions that influence the maximal contour due to stiction coming out of zero-velocity states.

Biaxial contour mappings were then generated for the same structure at multiple speeds, results for which are summarized in Table 6.1 and plotted in Figure 6.7. Figure 6.6 gives biaxial contour error mappings for some samples of these print speeds.

Table 6.1 PI controllers designed in simulation using the system models for each axis.

Biaxial Contour Error	1 mm/s	2 mm/s	5 mm/s	8 mm/s	10 mm/s	12 mm/s	15 mm/s	20 mm/s	25 mm/s
Min (μm)	0.035	0.045	0.066	2.58	4.87	1.18	2.59	2.53	6.65
Max (μm)	41.7	62.4	92.2	104	109	105	111	130	155
Avg (μm)	4.16	7.16	18.6	28.9	35.7	36.8	40.5	48.5	62

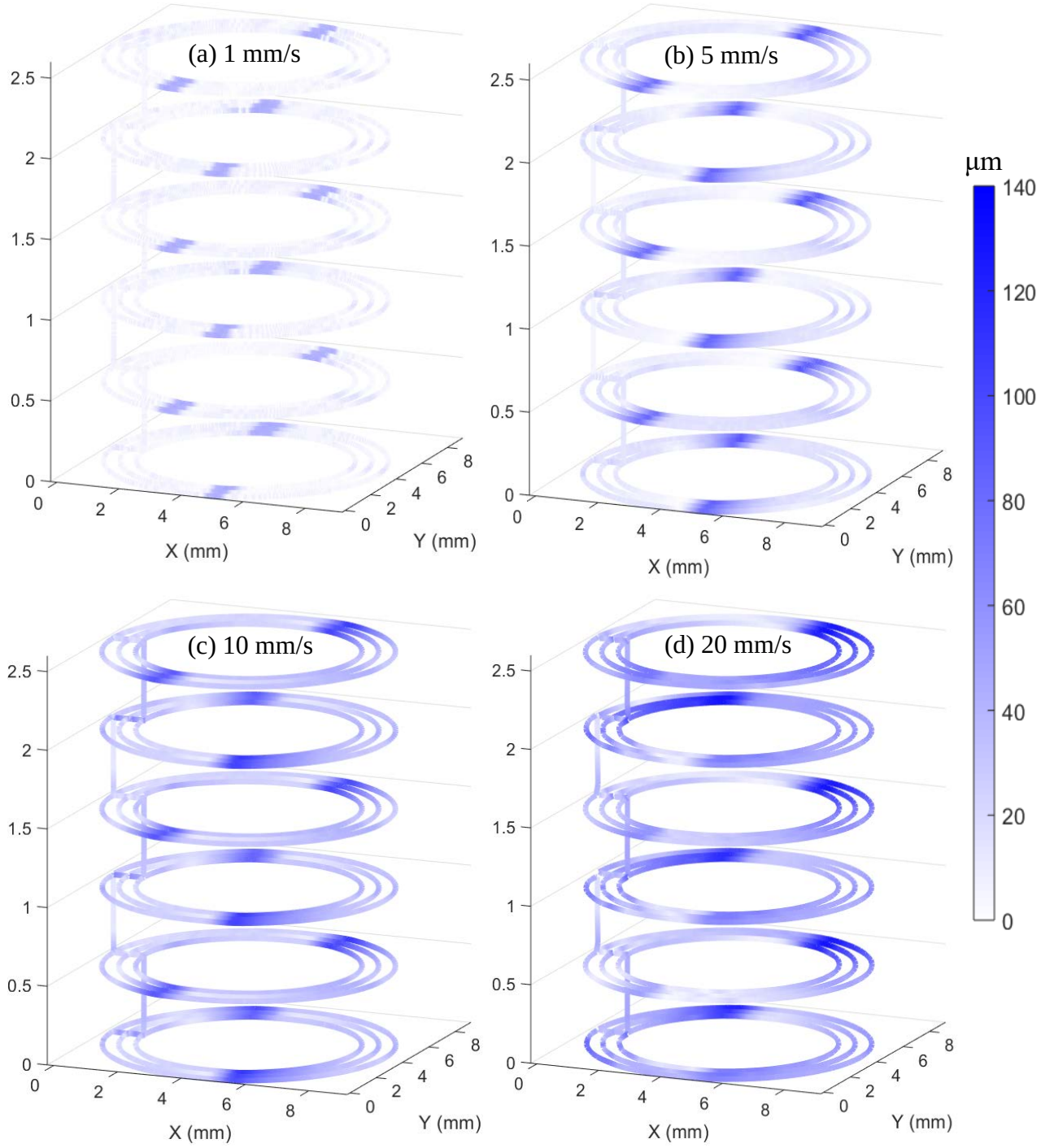

Figure 6.7 Biaxial contour error maps for print speeds of (a) 1 mm/s, (b) 5 mm/s, (c) 10 mm/s, (d) 20 mm/s. Scale bars indicate intensity of biaxial contour error in μm and are imposed uniformly on all figures. (a) is a reprinting of Figure 6.4 under the new scaling.

Figure 6.6 and 6.7 illustrate how the biaxial contour errors generally increase with the printing speed. Except for the 8-10 mm/s range, this relation is nearly monotonically increasing which one could expect. The minimum and average values have a linear trend. The maximum values behave similar to a power root response $(x^{1/p})$ until 16 mm/s when it enters a linear region. One can also observe from Figure 6.6 that the regions of maximal error discussed above are present across the range of speeds.

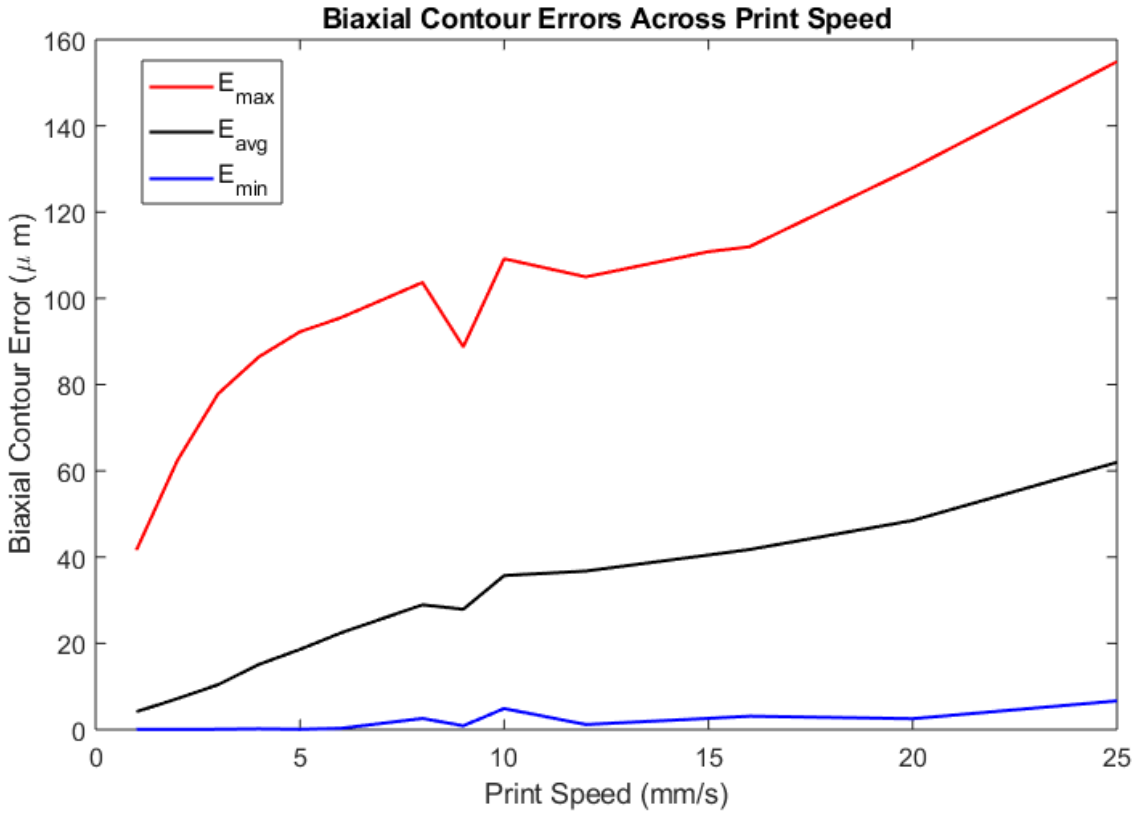

Figure 6.8 Biaxial contour error values (max, min, and average) plotted across various printing speeds from 1-25 mm/s

For print speeds up to 25mm/s the maximum errors all fall under 250 μm and the average values fall under 100 μm. This author posits that this is a strong evidence to support the claim for a well-tuned and high performing controller on the μRD system.

6.3 Fabricated Magnetic Cores

This section showcases the results of the tuned μRD system's fabrication abilities. The previous section described the effectiveness of the controller design to track the toolpaths used in the construction of these components. Fabrication for the components shown utilized a 500 μm dispensing tip to generate the 500 μm thick ink paths. There are no programmed gaps for the toroidal topologies given in the previous section which corresponds to 100% infill. As seen in Figures 6.4 and 6.6, these structures contain 6 layers of 3 concentric circles. The printing speed chosen for the samples shown in Figure 6.8 was 15 mm/s. The samples fabricated at this speed showed no gapping in the deposition process as desired. Curing of the parts was conducted at room temperature by leaving samples on the substrate for 6 hours with no change to external conditions.

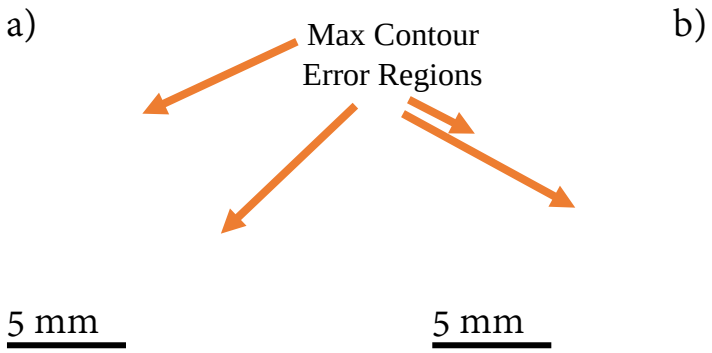

Figure 6.9 Example of a magnetic core fabricated by the μRD system. a) Top view of the core showing the concentric circles of the final layer. b) Same sample from the side showing the multiple layers of the AM process.

One can observe from Figure 6.8 a) the jagged regions containing the maximum biaxial contour errors from the mappings presented in section 6.2.1. By measuring several samples from these fabrication parameters, the average outer & inner diameters, and heights were established. The average outer diameter was found to be 9.34 mm; the average inner diameter was found to be 4.88 mm; the average height was found to be 3.21 mm. All samples fell within $\pm 100 \mu m$ of the average values for the inner and outer diameters while being within $\pm 50 \mu m$ of

the average height. The difference in average outer-inner radii gives the average wall thickness of 2.23 mm.

The high percent differences for the ID and wall thickness would indicate that there are errors affecting size beyond those introduced by the mechanical system alone. One such phenomena that was not considered during the design of this work is extrudate swelling. This is a phenomenon corresponding to extruded plastics in which the size of the rods/paths from the tip of the extruder are larger than the inner diameter of the nozzle as shown in Figure 6.9. Another possible explanation is thermal expansion occurring as the composites cure. Both are possible avenues that can be investigated in future works.

Additional parts were fabricated to the same height using only two concentric circles per layer to investigate their wall thicknesses. The desired wall thickness for these parts is 1.0 mm. Outer diameters were measured to be within the same range as the previous core samples. Measured thicknesses fell in a range of 1.43 – 1.59 mm with and average thickness of 1.52 mm for an average percent difference of 52.0%. This confirms there is material expansion from some source at nearly 50% from non-expanding expectations.

Table 6.2 Desired vs. average measured dimensions of fabricated samples

Dimension	Desired (mm)	Actual (Avg, mm)	% Diff
OD (mm)	9	9.34	3.78
ID (mm)	6	4.88	18.7
Height (mm)	3	3.21	7.00
Wall Thickness (mm)	1.5	2.23	48.7

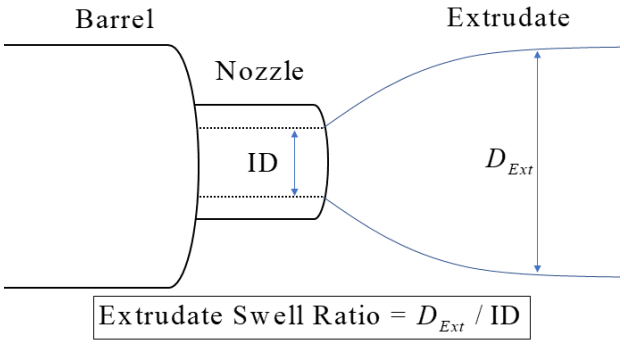

Figure 6.10 Conceptual diagram of extrudate swell

Chapter 7
Conclusions and Future Works

7.1 Summary of Results

This work developed a carbonyl iron-epoxy composite ink that was curable at room temperatures, far below that required of sintering methods. This analog ink was developed to investigate the feasibility of our μRD system to fabricate magnetic cores of toroidal topologies. A new auger valve extrusion system was installed on the system which negated a common need for controlling pneumatics during the manufacturing process.

Well-tuned PI controllers were designed and implemented on each axis of the μRD system to accurately track velocity profiles. A nominal position integrator was also implemented per axis to further increase the precision associated with the positioning system. The controllers designed for the X and Y-Axes are capable of tracking velocities within 2% at steady states with less than 20% overshoot. Settling times were imposed at 250 ms and were easily achieved by the controllers. The controller for the Z-Axes followed the same method of design; however, the objective was to track a steady-state position which is common for AM systems of this type. This controller is capable of tracking a steady state position to within 0.5% with a settling time window of 250 ms.

The magnetic components presented in this work show a feasible method for low-temperature fabrication of ferrite-epoxy composites by a material extrusion type AM technique. The target topologies of the AM process were square toroids with dimensions 9/6/3 mm at a resolution of 500 μm provided by the dispensing tip inner diameter. The AM process

was first evaluated in terms of the systems controller ability to track the toolpaths associated with this topology at varied speeds from 1-25 mm/s. Biaxial contour error mappings showed a specific region for which a maximal contour tracking error occurred and was present throughout the range of speeds. The mappings and data also showed a generally increasing trend of the error with speed. The maximum (average) biaxial contour error falling under 250 μm (100 μm) indicate good control performance for fabrication purposes.

Fabrication of components from the ferrite composite inks resulted in average dimensions of 9.34/4.88/3.21 mm. Inspection of wall thickness for 3 and 2 wall lines (concentric circles) show an average expansion of roughly 50% in the radial directions and 7% in the z-direction. The expansion was not formally addressed in this work but possible avenues for investigation were identified as extrudate swelling and thermal expansion effects. The fact that dimensions were larger than expected in all directions is a good result overall since it indicates proper material rheology was met for printing.

7.2 Future Work

Future works will aim at improving upon and/or expanding the capabilities established in this thesis. Areas for direct improvement include the materials and controls systems. This work focused on an analog composite ink to show the feasibility of additively manufacturing ferrite-composite inks under low temperature conditions. The use of superparamagnetic iron-oxide nanocomposites as a magnetic ink system will be a major focus for improvement of the materials development. Future work must inspect phenomena such as extrudate swelling far in advance of the manufacturing stage to mitigate dimensional deviations in fabrication.

While this work developed a well-tuned controller for the μRD system it employed, the capability of printing at higher and higher speeds with minimal error continues to be a demand for these types of manufacturing technologies. Future work pertaining to the controls and fabrication systems will improve upon the biaxial contour errors that are seen at higher printing speeds. One method for addressing this issue is implementation of advanced iterative learning control algorithms (ILC).

Efforts to expand upon the μRD system's capabilities will focus on three more aspects. First, additional form factors for inductive components will be investigated. There will be a strong push for topologies not realizable with standard manufacturing techniques. Second, closed-loop feedback and control of the extrusion system will be developed in the hopes of further improving the control of material deposition characteristics. Lastly, additional extruder systems should be added to the existing system in order to bring multiple materials to the fabrication process of these components. This could allow for additive manufacturing of complete magnetic devices – including winding elements – to be fabricated in a single step; opening the door to manufacturing these components directly on to power supply modules.

References

[1] J. W. Stansbury and M. J. Idacavage, “3D printing with polymers: Challenges among expanding options and opportunities,” in *Dental Materials*, 2016.

[2] “Introduction to CNC machining | 3D Hubs.” [Online]. Available: https://www.3dhubs.com/knowledge-base/cnc-machining-manufacturing-technology-explained#what. [Accessed: 10-Oct-2018].

[3] “Opportunities, Challenges, and Policy Implications of Additive Manufacturing 3D Printing United States Government Accountability Office,” 2015.

[4] S. V Atre, T. J. Weaver, and R. M. German, “982417 Injection Molding of Metals and Ceramics.”

[5] “Metal Powder Injection Molding › Chair of Materials Science and Engineering for Metals.” [Online]. Available: https://www.wtm.tf.fau.eu/forschung/hochtemperaturwerkstoffe/prozesstechnik/metal-powder-injection-molding/. [Accessed: 10-Oct-2018].

[6] K. Eiamsa-Ard and K. Wannissorn, “Conformal bubbler cooling for molds by metal deposition process,” *CAD Comput. Aided Des.*, vol. 69, pp. 126–133, 2015.

[7] “Metal Powder Injection Moulding › Welcome to ZMP.” [Online]. Available: https://www.zmp.fau.de/forschung/metal-powder-injection-moulding/. [Accessed: 30-Oct-2018].

[8] “Standard Terminology for.”

[9] C. W. Hull and C. Arcadia, “United States Patent (19) Hull (54) (75) (73) 21) 22 (51) 52) (58) (56) APPARATUS FOR PRODUCTION OF THREE-DMENSONAL OBJECTS BY STEREO THOGRAPHY.”

[10] W. A. INC, “3D Printing and Additive Manufacturing State of the Industry.”

[11] X. Wang, M. Jiang, Z. Zhou, J. Gou, and D. Hui, “3D printing of polymer matrix composites: A review and prospective,” *Composites Part B: Engineering*. 2017.

[12] S. Mellor, L. Hao, and D. Zhang, “Additive manufacturing: A framework for implementation,” in *International Journal of Production Economics*, 2014.

[13] B. Ahuja, M. Karg, and M. Schmidt, “Additive manufacturing in production: challenges and opportunities,” 2015, vol. 9353, p. 935304.

[14] M. K. Thompson *et al.*, “Design for Additive Manufacturing: Trends, opportunities, considerations, and constraints,” *CIRP Ann. - Manuf. Technol.*, 2016.

[15] I. Gibson, D. W. Rosen, and B. Stucker, *Additive Manufacturing Technologies: Rapid Prototyping to Direct Digital Manufacturing*. Springer, 2010.

[16] S. Singh, S. Ramakrishna, and R. Singh, “Material issues in additive manufacturing: A review,” *Journal of Manufacturing Processes*. 2017.

[17] N. Hopkinson, R. J. M. Hague, P. M. Dickens, and J. Wiley, *Rapid Manufacturing An Industrial Revolution for the Digital Age*. .

[18] “Laminated Object Manufacturing (LOM).” [Online]. Available: https://www.custompartnet.com/wu/laminated-object-manufacturing. [Accessed: 10-Oct-2018].

[19] “Carbon - The Future of 3D Manufacturing Printers & Systems.” [Online]. Available: https://www.carbon3d.com/. [Accessed: 30-Oct-2018].

[20] “Metal 3D Printing: Laser Sintering vs. Bulk Sintering in a Furnace – Pros and Cons | 3DPrint.com | The Voice of 3D Printing / Additive Manufacturing.” [Online]. Available: https://3dprint.com/193946/laser-sintering-vs-bulk-sintering/. [Accessed: 30-Oct-2018].

[21] F. Wirth, S. Arpagaus, and K. Wegener, “Analysis of melt pool dynamics in laser cladding and direct metal deposition by automated high-speed camera image evaluation,” *Addit. Manuf.*, vol. 21, pp. 369–382, May 2018.

[22] D. Kim, H. Lee, S. Jeong, and J. Moon, “All-Ink-Jet Printed Flexible Organic Thin-Film Transistors on Plastic Substrates,” 2018.

[23] “Metal 3D Printing Processes - Metal Extrusion FFF/FDM.” [Online]. Available: https://news.3deo.co/metal-3d-printing-processes-fdm-fff. [Accessed: 30-Oct-2018].

[24] R. D. Farahani, K. Chizari, and D. Therriault, “Three-dimensional printing of freeform helical microstructures: a review,” 2014.

[25] T. Billiet, M. Vandenhaute, J. Schelfhout, S. Van Vlierberghe, and P. Dubruel, “A review of trends and limitations in hydrogel-rapid prototyping for tissue engineering,” *Biomaterials*, vol. 33, pp. 6020–6041, 2012.

[26] R. D. Farahani, R. D. Farahani, L. L. Lebel, and D. Therriault, “Processing parameters investigation for the fabrication of self-supported and freeform polymeric microstructures using ultraviolet-assisted three-dimensional printing Recent citations Processing parameters investigation for the fabrication of self-supported and freeform polymeric microstructures using ultraviolet-assisted three-dimensional printing,” *J. Micromechanics Microengineering J. Micromech. Microeng*, vol. 24, p. 12, 2014.

[27] S. V Murphy and A. Atala, “3D bioprinting of tissues and organs,” *Nat. Biotechnol.*, vol. 32, no. 8, 2014.

[28] G. N. Levy, R. Schindel, and J. P. Kruth, “RAPID MANUFACTURING AND RAPID TOOLING WITH LAYER MANUFACTURING (LM) TECHNOLOGIES, STATE OF THE ART AND FUTURE PERSPECTIVES.”

[29] J. Y. Lee, J. An, and C. K. Chua, “Fundamentals and applications of 3D printing for novel materials,” *Applied Materials Today*. 2017.

[30] H. Gu *et al.*, “An overview of multifunctional epoxy nanocomposites,” *J. Mater. Chem. C*, vol. 4, p. 5890, 2016.

[31] H. W. Tan, T. Tran, and C. K. Chua, “A review of printed passive electronic components through fully additive manufacturing methods,” *Virtual and Physical Prototyping*. 2016.

[32] E. Kroll and D. Artzi, “Rapid Prototyping Journal Enhancing aerospace engineering students’ learning with 3D printing wind-tunnel models Article information.”

[33] S. Yuan, J. Bai, C. Kai Chua, K. Zhou, and J. Wei, “Characterization of Creeping and Shape Memory Effect in Laser Sintered Thermoplastic Polyurethane,” 2016.

[34] S. Yuan, J. Bai, C. K. Chua, J. Wei, and K. Zhou, “Material evaluation and process optimization of CNT-coated polymer powders for selective laser sintering,” *Polymers (Basel).*, vol. 8, no. 10, 2016.

[35] S. Yuan, J. Bai, C. Kai Chua, J. Wei, and K. Zhou, “Highly enhanced thermal conductivity of thermoplastic nanocomposites with a low mass fraction of MWCNTs by a facilitated latex approach,” 2016.

[36] H. Chung and S. Das, “Processing and properties of glass bead particulate-filled functionally graded Nylon-11 composites produced by selective laser sintering,” 2006.

[37] M. Nikzad, S. H. Masood, and I. Sbarski, “Thermo-mechanical properties of a highly filled polymeric composites for Fused Deposition Modeling,” *Mater. Des.*, vol. 32, pp. 3448–3456, 2011.

[38] K. Boparai, R. Singh, and H. Singh, “Comparison of tribological behaviour for Nylon6-Al-Al2O3 and ABS parts fabricated by fused deposition modelling: this paper reports a low cost composite material that is more wear-resistant than conventional ABS,” *Virtual Phys. PrototypingPhys Prototyp*, vol. 10, no. 2, pp. 55–66, 2015.

[39] D. V Isakov, Q. Lei, F. Castles, C. J. Stevens, C. R. M. Grovenor, and P. S. Grant, “3D printed anisotropic dielectric composite with meta-material features,” *JMADE*, vol. 93, pp. 423–430, 2016.

[40] M. Kurimoto, Y. Yamashita, H. Ozaki, T. Kato, T. Funabashi, and Y. Suzuoki, “3D printing of conical insulating spacer using alumina /UV-cured-resin composite,” in *2015 IEEE Conference on Electrical Insulation and Dielectric Phenomena (CEIDP)*, 2015, pp. 463–466.

[41] C. M. Shemelya *et al.*, “Mechanical, Electromagnetic, and X-ray Shielding Characterization of a 3D Printable Tungsten-Polycarbonate Polymer Matrix Composite for Space-Based Applications.”

[42] S. H. Masood and W. Q. Song, “Development of new metal/polymer materials for rapid tooling using Fused deposition modelling.”

[43] J. D. Venables, “Review Adhesion and durability of metal-polymer bonds.”

[44] M. Nikzad, S. H. Masood, I. Sbarski, and A. Groth, “Thermo-Mechanical Properties of a Metal-filled Polymer Composite for Fused Deposition Modelling Applications,” 2007.

[45] D. Mishra, Pm. Raj, and R. Tummala, “Design, fabrication and characterization of thin power inductors with multilayered ferromagnetic-polymer composite structures,”

MEE, vol. 160, pp. 34–38, 2016.

[46] A. FUJITA, Y. FUKUDA, K. NISHIZAWA, and J. TOGAWA, “JFE Technical Report No.8.”

[47] J. Watt *et al.*, “Gram scale synthesis of Fe/FexOy core–shell nanoparticles and their incorporation into matrix-free superparamagnetic nanocomposites,” *J. Mater. Res.*, vol. 33, no. 15, pp. 2156–2167, Aug. 2018.

[48] R. Lebourgeois, E. Labouré, Y. Lembeye, and J.-P. Ferrieux, “LTCC magnetic components for high density power converter,” *AIP Adv.*, vol. 8, no. 4, p. 047901, Apr. 2018.

[49] Y. Yan *et al.*, “Additive Manufacturing of Magnetic Components for Heterogeneous Integration,” *2017 IEEE 67th Electron. Components Technol. Conf.*, pp. 324–330, 2017.

[50] Y. Yan, J. Moss, K. D. T. Ngo, Y. Mei, and G. Q. Lu, “Additive Manufacturing of Toroid Inductor for Power Electronics Applications,” *IEEE Trans. Ind. Appl.*, vol. 53, no. 6, pp. 5709–5714, 2017.

[51] Y. Yan, “Design Methodology and Materials for Additive Manufacturing of Magnetic Components,” 2017.

[52] S. Balci, I. Sefa, and N. Altin, “Thermal Behavior of a Medium-Frequency Ferrite-Core Power Transformer,” *J. Electron. Mater.*, vol. 45, no. 8, pp. 3978–3988, Aug. 2016.

[53] D. Bhalla, D. K. Singh, S. Singh, and D. Seth, “Material Processing Technology for Soft Ferrites Manufacturing,” *Am. J. Mater. Sci.*, vol. 2012, no. 6, pp. 165–170, 2012.

[54] D. A. Hewitt, “Approaches to improving thermal performance of inductors with a view to improving power density A thesis submitted by The Department of Electronic and Electrical Engineering at The University of Sheffield Supervised by September 2015 Summary,” no. September, 2015.

[55] J. Y. Park and M. G. Allen, “Development of magnetic materials and processing techniques applicable to integrated micromagnetic devices,” *J. Micromechanics Microengineering J. Micromech. Microeng*, vol. 8, no. 98, pp. 307–316, 1998.

[56] H. Shokrollahi and K. Janghorban, “Soft magnetic composite materials (SMCs),” *J.*

Mater. Process. Technol., vol. 189, no. 1–3, pp. 1–12, Jul. 2007.

[57] I. P. Gilbert, V. Moorthy, S. J. Bull, J. T. Evans, and A. G. Jack, “Development of soft magnetic composites for low-loss applications,” *J. Magn. Magn. Mater.*, vol. 242–245, pp. 232–234, Apr. 2002.

[58] F. Fiorillo, E. Ferrara, M. Coïsson, C. Beatrice, and N. Banu, “Magnetic properties of soft ferrites and amorphous ribbons up to radiofrequencies,” *J. Magn. Magn. Mater.*, vol. 322, no. 9, pp. 1497–1504, 2010.

[59] B. Williams, “Soft Magnetic Materials-Inductors and Transformers,” in *Power Electronics: Devices, Drivers, Applications, and Passive Components*, 2006.

[60] M. Mu *et al.*, “High Frequency Magnetic Core Loss Study,” 2013.

[61] J. M. Silveyra, P. Xu, V. Keylin, V. DeGeorge, A. Leary, and M. E. McHenry, “Amorphous and Nanocomposite Materials for Energy-Efficient Electric Motors,” *J. Electron. Mater.*, vol. 45, no. 1, pp. 219–225, Jan. 2016.

[62] H. Shokrollahi and K. Janghorban, “Review Soft magnetic composite materials (SMCs),” *JMPT* , vol. 189, no. 1–3, pp. 1–12, 2007.

[63] “Magnetic Materials: Soft Magnets.”

[64] M. Bennet *et al.*, “Biologically controlled synthesis and assembly of magnetite nanoparticles,” *Faraday Discuss.*, vol. 181, no. 0, pp. 71–83, Jul. 2015.

[65] V. Marghussian and V. Marghussian, “Magnetic Properties of Nano-Glass Ceramics,” *Nano-Glass Ceram.*, pp. 181–223, Jan. 2015.

[66] S. Mori, T. Mitsuoka, M. Sonehara, T. Sato, and N. Matsushita, “High permeability and low loss of Ni-Zn-Fe ferrite/metal composite cores in high frequency region,” *AIP Adv.*, vol. 7, no. 5, p. 056657, May 2017.

[67] J. Xiao, J. U. Otaigbe, and D. C. Jiles, “Modeling of magnetic properties of polymer bonded Nd–Fe–B magnets with surface modifications,” *J. Magn. Magn. Mater.*, vol. 218, no. 1, pp. 60–66, Jul. 2000.

[68] E. Bayramlı, Ö. Gölgelioğlu, and H. B. Ertan, “Powder metal development for electrical motor applications,” *J. Mater. Process. Technol.*, vol. 161, no. 1–2, pp. 83–88, Apr. 2005.

[69] E. Enescu, P. Lungu, S. Marinescu, and P. Dragoi, “The effect of processing

conditions on magnetic and electric properties of composite materials used in nonconventional magnetic circuits," 2006.

[70] F.-L. Jin, X. Li, and S.-J. Park, "Synthesis and application of epoxy resins: A review," *J. Ind. Eng. Chem.*, vol. 29, pp. 1–11, Sep. 2015.

[71] B. G. Compton and J. A. Lewis, "3D-Printing of Lightweight Cellular Composites," *Adv. Mater.*, vol. 26, no. 34, pp. 5930–5935, Sep. 2014.

[72] Y. Sugawa, K. Ishidate, M. Sonehara, and T. Sato, "Carbonyl-Iron/Epoxy Composite Magnetic Core for Planar Power Inductor Used in Package-Level Power Grid," *IEEE Trans. Magn.*, vol. 49, no. 7, pp. 4172–4175, Jul. 2013.

[73] D. A. Bristow, "Modeling and control of a microscale robotic deposition manufacturing system," pp. 62–63, 2003.

[74] A. A. Armstrong, A. G. Alleyne, and A. W. Johnson, "MODELING AND CONTROL OF AN EASY-TO-USE DIRECT WRITE PRINTING SYSTEM FOR FABRICATION OF BONE SCAFFOLDS."

[75] D. J. Hoelzle, "Flexible adaptation of iterative learning control with applications to synthetic bone graft manufacturing," 2011.

[76] D. A. Bristow, "Iterative learning control for precision motion control of microscale and nanoscale tracking systems," *ProQuest Diss. Theses*, p. 154, 2007.

[77] AEROTECH, "Nservo Servo Controller | Aerotech, Inc." [Online]. Available: https://www.aerotech.com/product-catalog/drives-and-drive-racks/nservo.aspx. [Accessed: 10-Oct-2018].

[78] Laser-Components, "Nservo - Digital Controller Module." .

[79] J. A. Lewis, J. E. Smay, J. Stuecker, and J. Cesarano, "Direct ink writing of three-dimensional ceramic structures," *Journal of the American Ceramic Society*, vol. 89, no. 12. pp. 3599–3609, 2006.

[80] S. J. Adamson, A. Lewis, D. Ashley, and B. Schmaltz, "New Piezo Actuated Dispensing Method for Consistent Solder Paste Dots."

[81] G. Otten, G. Otten, T. J. A. De Vries, A. M. Rankers, and E. W. Gaal, "Linear Motor Motion Control Using a Learning Feedforward Controller," *IEEE/ASME Trans. MECHATRONICS*, vol. 2, pp. 179--187, 1997.

[82] D. C. Hanselman, *Brushless Permanent-Magnet Motor Design*. New York, NY: McGraw-Hill, Inc., 1994.

[83] T. Zieliński and K. Duda, “Frequency and Damping Estimation Methods - An Overview,” *Metrol. Meas. Syst.*, vol. 18, no. 4, pp. 505–528, 2011.

[84] K. Prasertwong and N. Mithulananthan, “A new algorithm based on logarithm decrement to estimate the damping ratio for power system oscillation,” in *2017 14th International Conference on Electrical Engineering/Electronics, Computer, Telecommunications and Information Technology (ECTI-CON)*, 2017, pp. 517–520.

[85] J. Soni and S. Roy, “Design and characterization of a nano-Newton resolution thrust stand,” *Cit. Rev. Sci. Instrum*, vol. 84, p. 95103, 2013.

[86] C. Ge and S. Sutherland, “Application of Experimental Modal Analysis to Determine Damping Properties for Stacked Corrugated Boxes,” *Math. Probl. Eng.*, vol. 2013, pp. 1–8, Jun. 2013.